Kovove Mater. 61 2023 285–305
DOI: 10.31577/km.2023.5.285

Fatigue crack growth behavior of Al 2014 alloy subjected to cryogenic rolling and post-rolled annealing

Amit Joshi[1]*, K. K. Yogesha[2], Sunil Chamoli[1], Rengaswamy Jayaganthan[3], Gbadebo Moses Owolabi[4]

[1] *Department of Mechanical Engineering, G. B. Pant Institute of Engineering & Technology Pauri (Garhwal), National Institute of Engineering, Mysuru-570008, India*
[2] *Department of Mechanical Engineering, Indian Institute of Technology Madras, Chennai-600036, India*
[3] *Department of Engineering Design, Indian Institute of Technology Madras, Chennai-600036, India*
[4] *Department of Mechanical Engineering, Howard University, Washington, DC, USA*

Received 14 December 2022, received in revised form 2 May 2023, accepted 12 May 2023

Abstract

The present study investigated grain growth, recrystallization, and fatigue crack growth behavior of Al-Cu-Si alloy subjected to cryorolling and annealing treatment for 1 h. Temperature from 373 to 523 K was considered for this study. Cryorolling is used to produce ultra-fine-grained (UFG) structures, while annealing is used to study the recrystallization and grain growth. The fatigue crack growth (FCG) rate was measured in the low-stress intensity factor range (ΔK) (Stage II) and high-stress intensity factor ranges using the Paris equation and measuring the striation width. The results discovered that cryorolling led to a significant decrease in the fatigue crack growth resistance in the low-stress intensity factor range compared to coarse grain counterparts due to a decrease in the crack closure level in the cryorolled alloy. The results also showed that the fatigue crack growth resistance of the cryorolled alloy improved in the high-stress intensity factor range due to the formation of ultra-fine-grained microstructure, resulting in fine striations observed from the fractographic studies. The post-annealed samples at 373 K exhibited higher fatigue crack growth resistance in low and high-stress intensity factor ranges. High fatigue crack growth resistance in the annealed sample in low and high-stress intensity factor range is attributed to the fine semicoherent spherical phase θ'.

K e y w o r d s: Al alloys, cryorolling, annealing, fatigue crack growth rate, fractography

Nomenclature

– $\mathrm{d}a/\mathrm{d}N$ is crack growth rate (mm/cycle),
– ΔK is the stress intensity factor range,
– r_{rp} is the radius of the cyclic plastic zone near the crack tip,
– ΔK_{eff} is an effective stress intensity factor range.

1. Introduction

Ultrafine-grained (UFG) materials produced through severe plastic deformation (SPD) methods have been thoroughly studied for more than a decade [1]. The significant improvement in the mechanical properties achieved in the UFG material fabricated by SPD methods has attracted much attention to commercializing these materials for high-strength applications such as automotive, aerospace, and structural sectors [2–4]. However, to facilitate the widespread use of UFG materials, the damage tolerance properties such as fracture toughness, fatigue resistance, and fatigue crack growth (FCG) behavior should be addressed critically to ensure damage safe design of mechanical components subjected to cyclic loading

*Corresponding author: e-mail address: amitiitrebsd@gmail.com

[5]. Moreover, understanding the fatigue properties of UFG metals/alloys is essential because the formation of cracks with subsequent propagation under fatigue loading could lead to a catastrophic failure of structural components during service conditions without providing a previous warning [6].

Several studies have focused on analyzing the deformation behavior of UFG materials. It has been shown that monotonic strength properties have significantly improved if the grain size is reduced well below 1 μm. This improvement in the monotonic strength properties of UFG metals/alloys may be due to the enhancement of local plastic deformation energy, which is the energy required to move the dislocations inside the grain [7]. With more energy needed for the direction of the dislocations, the yield strength of the metals and alloys increases [7]. The dependence of monotonic strength properties on the grain size has also been expressed mathematically via the famous Hall-Petch relationship represented by the following equation [5]:

$$\sigma_{\mathrm{y}} = \sigma_0 + kD^{-1/2}, \tag{1}$$

where σ_{y} is the yield stress, σ_0 is the lattice friction stress, k is the Hall-Petch constant, and D is the grain size. Based on this, it may be mentioned that monotonic strength properties such as the tensile strength, the yield strength, and the ductility-related issues of UFG metals/alloys were significantly explored in the published literature [8–10]. However, research studies focusing on the effect of grain size on cyclic plasticity, fatigue life, and the fatigue crack propagation behavior of UFG metal/alloy are very limited in the literature.

Hanlon et al. [6] reported that high cycle fatigue (HCF) resistance of the metals/alloys increases when the grain size is reduced to less than 1 μm at the expense of fatigue crack growth rate (FCGR). Cavaliere [11] conducted an extensive review of the fatigue behavior of these materials. The author reported that the HCF strength of NC material has improved with lessening grain size, while its susceptibility to crack initiation decreases on refining the grains well below 1 μm. However, the low cycle fatigue (LCF) strength of finer grain materials developed by SPD processing deteriorates with a reduction in grain size [11]. Similar studies were stated by Hoppel et al. during the strain-controlled test of various UFG metals and alloys such as Cu, Al, Al 6061, and α-brass [12, 13].

Hanlon et al. [6] reported that high cycle fatigue (HCF) resistance of the metals/alloys increases when the grain size is reduced to less than 1 μm at the expense of the FCG rate. Cavaliere [11] conducted an extensive review of the fatigue behavior of these materials. The author reported that the HCF strength of NC material improved with lessening grain size, while its susceptibility to crack initiation decreased on refining the grains well below 1 μm. However, the low cycle fatigue (LCF) strength of finer grain materials developed by SPD processing deteriorates with a reduction in grain size [11]. Hoppel et al. [12, 13] reported similar results during the strain-controlled test of various UFG metals and alloys such as Cu, Al, Al 6061, and α-brass.

The comparison between the fatigue life of UFG metals and coarse grain (CG) metals and alloys can be well explained by the total strain fatigue life diagram reported in a review paper by Mughrabi and Hoppel [5]. The following equations are used for understanding the total strain fatigue life diagram:

$$\frac{\Delta\varepsilon_{\mathrm{t}}}{2} = \frac{\Delta\varepsilon_{\mathrm{el}}}{2} + \frac{\Delta\varepsilon_{\mathrm{pl}}}{2}, \tag{2}$$

$$\frac{\Delta\varepsilon_{\mathrm{t}}}{2} = \frac{\sigma'_{\mathrm{f}}}{E}\left(2N_{\mathrm{f}}\right)^b + \varepsilon'_{\mathrm{f}}\left(2N_{\mathrm{f}}\right)^c, \tag{3}$$

where $\Delta\varepsilon_{\mathrm{t}}$, $\Delta\varepsilon_{\mathrm{el}}$, and $\Delta\varepsilon_{\mathrm{pl}}$ are the total, elastic, and plastic strain ranges, respectively, σ'_{f} is known as the fatigue strength coefficient, $2N_{\mathrm{f}}$ is the number of load reversals/cycles before failure, $\varepsilon'_{\mathrm{f}}$ and b are called fatigue ductility coefficient and strength exponent, respectively, and c is the fatigue ductility exponent. A material's total strain fatigue life comprises HCF and LCF regimes, as illustrated in Fig. 1a. On comparing the first term of Eq. (2) and Eq. (3), the equation for the HCF regime is obtained, known as Basquin law, and expressed as per the following equation:

$$\sigma_{\mathrm{a}} = \frac{\Delta\varepsilon}{2}E = \sigma'_{\mathrm{f}}\left(2N_{\mathrm{f}}\right)^b. \tag{4}$$

For the LCF regime, the well-known Coffin-Manson relationship is used, which is obtained by comparing the second term of Eq. (2) and Eq. (3) and can be expressed by the following equation:

$$\frac{\Delta\varepsilon_{\mathrm{pl}}}{2} = \varepsilon'_{\mathrm{f}}\left(2N_{\mathrm{f}}\right)^c. \tag{5}$$

It is testified that the life of metals and alloys under cyclic load largely depends on the growth life of fatigue crack. Therefore, the crack propagation behavior of UFG material must be investigated [14]. Patlan et al. [15] studied the FCG behavior of bulk UFG 5056 Al-Mg alloy processed by equal channel angular pressing (ECAP). The FCG behavior of ECAP-processed Al-Mg alloy was observed to be more at small stress intensity factor ranges ΔK than that of the coarse grain (CG) counterpart. The serrated crack profile and zigzag crack growth were found to be a primary mechanism associated with the CG alloy, resulting in a reduced FCG in the CG alloy, as described in their work. Chung et al. [16] investigated the FCG behavior of Al

6061 alloy processed by ECAP and compared the fatigue crack growth (FCG) behavior of the bulk U.F.G. Al 6061 alloy with its CG counterparts. The ECAP-processed alloy was observed to have a lower fatigue threshold and fatigue crack growth (FCG) rate than the unprocessed CG alloy in their work [16]. It was reported in their study that cracks path tortuosity has a significant role in blunting the crack propagation path of the unprocessed alloy resulting in a reduced fatigue crack growth rate (FCGR) of unprocessed Al 6061 alloy. Recently Meyer et al. [17] studied the crack growth behavior of 2-pass and 8-pass ECAP processed Al 6063 alloy and compared its FCG behavior with its CG counterparts. The CG alloy was observed to have a higher fatigue threshold and lower crack growth rate, as reported, while for the UFG alloy, a lower fatigue threshold along with a fatigue crack growth rate was measured. This is attributed to the higher crack path deflection and larger crack driving force for crack propagation in the CG alloy than in the bulk UFG alloy [17]. Although the FCG behavior of UFG metals/alloys has been investigated earlier, a generalized statement about the fatigue crack propagation behavior of UFG metals/alloys cannot be made since opposing trends of FCGR were also reported. Collini et al. [18] studied and compared the fatigue crack growth resistance of ECAP-processed UFG Cu with the CG one and found that the fatigue crack growth resistance of the UFG Cu was higher than that of the CG, especially at high ΔK. Similar trends were reported by Das et al. [19] during FCGR testing of bulk U.F.G. Al 7075 alloy processed through CR. As reported in their work, the diffused crack branching mechanism was the preliminary reason for the enhanced FCG resistance of bulk UFG alloy.

Zakaria et al. [20] examined the impact of annealing followed by solution treatment on the formation of initial structure influencing microstructure formation and resulting mechanical and corrosion properties in Al 1100 alloy. According to the results, solution and annealing treatments before cryorolling can give better microstructure and mechanical properties. Zheng et al. [21] achieved high strength and ductility in a heterogeneous-grain-structured CrCoNi alloy prepared by cryorolling and subsequent short-annealing. Wu et al. [22] explored the mechanical properties and microstructures of a CoCrFeNiMn high-entropy alloy obtained by cryorolling followed by annealing at 223 K. They reported recrystallization of cryorolled samples via a sub-grain migration during subsequent annealing. Yu et al. [23] proposed a trade-off between toughness and strength for Ti-6Al-4V titanium alloy using an amalgamation of cryorolling with short-period vacuum annealing. They found the weakening of the shear band structure after annealing, which significantly improves toughness.

Based on the above discussions, it is noted that a significant number of investigations relating to the HCF, LCF, and FCG behavior of UFG materials have focused on the ECAP-processed Ti, Ni, Cu, pure Al, and Al-Mg alloys. However, the FCG behavior of bulk UFG precipitation hardenable Al alloys deformed through other SPD methods is rare in the literature. These residues interact with the dislocations during the deformation and provide a strengthening effect, as reported [24–26]. The impact of precipitation on the monotonic strength properties of bulk U.F.G. Al 6061, Al 6063, and Al 7075 has been reported in [27–29]. However, the influence of post-deformation annealing on the fatigue and fracture behavior of bulk U.F.G. Al 2xxx series alloys, especially Al 2014 alloy developed by cryorolling, has not been studied in detail. Recently, the effect of precipitation on the HCF behavior of the cryorolled Al 2014 alloy has been reported in our earlier work, and we found that fine spherical phase θ' (Al_2Cu) significantly improves fatigue life [30]. However, the crack growth behavior of the cryorolled as well as post-annealed cryorolled Al 2014, has not been studied in detail. The principal alloying elements in precipitation hardenable Al 2014 alloy are Cu, Si, Mg, and Mn and are widely used in aircraft, automotive, and structural applications. Therefore, the present work investigated the effect of cryorolling and post-deformation annealing in the temperature range from 423 to 523 K on the fatigue crack growth rate of bulk U.F.G. Al 2014 alloy. The FESEM and TEM characterized microstructural features of the processed Al alloy to elucidate the fatigue crack propagation behavior of the deformed Al 2014 alloy.

2. Experimental

2.1. Experimental procedure

The chemical composition of the Al 2014 alloy used in the research work is presented in Table 1. The Al 2014 alloy plate of 40 mm thickness is procured from BAM PVT. Ltd., Mumbai, India, and is transformed into samples of dimensions 90 mm × 65 mm × 25 mm. These samples are then solution treated at 778 K for 2 h. They were processed by cryorolling up to a true strain 1.2 to produce UFG microstructure in the starting solutionized Al 2014 alloy. The detailed cryorolling procedure can be found in [30]. These deformed samples were annealed from 373 to 523 K with an interval of 323 K for 1 h. The mechanical properties (tensile strength, yield strength, and the % elongation) of the solution treated (ST), cryorolled, and annealed alloy were evaluated by executing a tensile test using the H25K-S Tinius Oslen tensile testing machine with a strain rate of $5 \times 10^{-4}\,s^{-1}$ and a constant crosshead speed. The total strain fatigue life diagram of a UFG

Table 1. Combination of chemical elements of Al 2014 alloy

Constituent	Cu	Si	Mg	Mn	Fe	Ti	Zn	Ni	Rest
(%)	4.5	0.77	0.44	0.71	0.20	0.05	0.06	0.009	Al

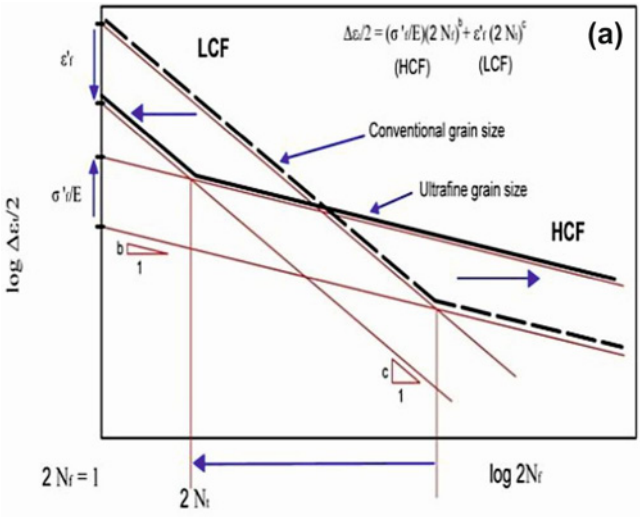

Fig. 1. (a) Total strain fatigue life diagram and (b) dimensions of CT sample used in this work.

material is shown in Fig. 1a. The FCGR tests were accomplished using compact tension (CT) specimen shown in Fig. 1b using ASTM 647-08 standards for the solution treated samples, cryorolled samples, and cryorolled annealed samples. The FCGR and a $\mathrm{d}a/\mathrm{d}N$ test were performed using the notched specimen subjected to cyclic loading and acceptably pre-cracked in fatigue. The FCGR, $\mathrm{d}a/\mathrm{d}N$, is articulated as a function of ΔK. The stress ratio (R-ratio ($\sigma_{\min}/\sigma_{\max}$)) for all samples during the FCGR tests was preserved at 0.1. Clevis loading fixtures were used for the CT specimens subjected to tensile-tensile fatigue, as described in [19]. The FCGR test was started by conducting fatigue pre-cracking up to .10 B, h, or 1 mm, whichever was greater, and growing the pre-crack in such a way that the final $K_{\max}$ during pre-cracking could not exceed the initial $K_{\max}$ under existing loading conditions, i.e., frequency 20 Hz, $R = 0.1$, initial and final crack sizes of 15 and 25 mm, respectively. A constant force amplitude test procedure was used to determine the crack growth rate in accordance with ASTM 647-08 standard. During the constant force amplitude test, each sample of the ST, CR, and CR + AN alloys was tested at a constant force range (ΔP) under a given loading condition. ΔK increasing values were used for finding out $\mathrm{d}a/\mathrm{d}N$ values, crack growth rate, and the unknowns C and m values in the Paris equation $\mathrm{d}a/\mathrm{d}N = C\Delta K^m$.

The microstructural features of solution treated, cryorolled, and cryorolled annealed samples were characterized by an optical microscope, TEM, and EBSD. The TEM sample preparation details were explained in [30]. EBSD samples were prepared by mechanical polishing with the help of fine cloth and followed by electro-polishing using an etchant having a composition of 80 % methanol and 20 % nitric acid at 13 V for 60 s. A step size of 0.05 μm was used for the entire processed sample in the present study during the EBSD scans. The fracture surface morphology of the FCGR tested samples for all processed conditions was examined by FE SEM Quanta 200.

2.2. Cryorolling

A metalworking procedure called cryorolling, commonly called cold rolling under cryogenic circumstances, involves thinning out a metal sheet or strip at extremely low temperatures. While the process of cryorolling is similar to that of conventional cold rolling, the rolling is done at temperatures below the metal's ductile-to-brittle transition temperature. This transition temperature might range from –70 to –150 ℃, depending on the particular metal.

During the cryorolling process, the metal is cooled to the required temperature using a cryogenic fluid, like liquid helium or liquid nitrogen. The thickness of the metal is further decreased by rolling it through several mills. The metal becomes less ductile at the cryogenic temperature, becoming more brittle and easily deformed.

Compared to conventional cold rolling, this leads to a higher reduction in thickness per pass.

Metals, including aluminum, copper, and stainless steel, can be cryorolled to enhance their mechanical

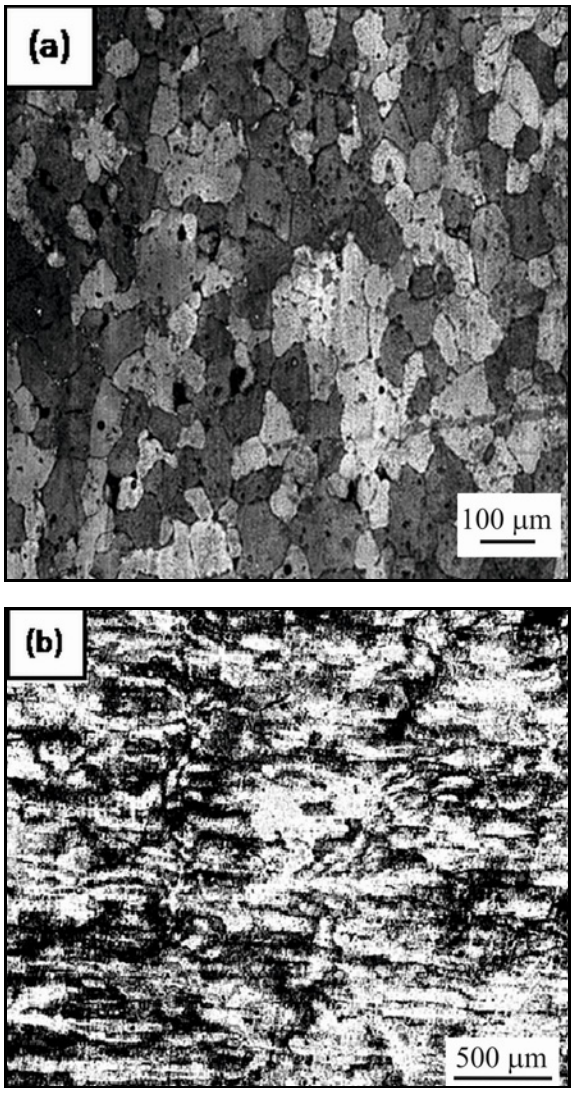

Fig. 2. Optical micrograph of Al 2014 alloy: (a) solution treated and (b) cryorolled 75 %.

qualities. The procedure can lead to improved surface quality, dimensional correctness, and increased strength, hardness, and fatigue resistance. Metals can be cryorolled to create ultra-fine grain formations, enhancing their mechanical characteristics even more.

Cryogenic fluids must be used, necessitating specialized tools and knowledge, and can be costly and dangerous if not handled appropriately. They are frequently employed in aerospace, automotive, and medicine, where high-performance materials are necessary.

3. Results

3.1. Optical microstructure

Optical microscopy was used to characterize the microstructural features of the solution treated and cryorolled Al 2014 alloy. Figure 2a corresponds to the optical microstructure of the starting solution treated alloy. The slightly equiaxed microstructure with a grain size of 50–200 μm can be visualized in the figure. When solution treated Al 2014 alloy is cryorolled up to a true strain of 1.3, the coarser grains in the solution treated alloy are transformed into an elongated substructure, severely deformed with a low aspect ratio as observed from Fig. 2b. Usually, optical microscopic studies in severely impaired alloy do not provide the information regarding dislocation sub-structure formed along with the quantification of high angle and low angle grain boundaries during the deformation. Therefore, this work characterized microstructural features of high-strain samples (i.e., deformed samples) with the help of TEM and EBSD.

3.2. EBSD studies

Microstructural evolution in the cryorolled and cryorolled annealed Al 2014 alloy in the temperature range of 373 to 523 K was investigated by performing EBSD studies on the corresponding samples in the present work. The inverse pole figure (IPF) map is superimposed with grain rotation (GR) angles, as shown in Fig. 3. Figure 3a shows the IPF map of the cryorolled sample. Severe deformation imposed by cryorolling can be observed in this figure. In addition, severely deformed and elongated substructures with a low aspect ratio along the rolling direction can be identified in Fig. 3a for the cryorolled sample. The GR angle superimposed on Fig. 3a can be divided into three parts: (i) 2°–5° (misorientations, dislocations, and very low angle grain boundaries), (ii) 5°–15° (low angle grain boundaries), and (iii) $> 15°$ (high angle grain boundaries). A high fraction of misorientation with very low angle grain boundaries and dislocations was observed in Fig. 3a for the cryorolled sample. When the cryorolled sample is annealed at 373 K, a slight decrease in the fraction of low angle grain boundaries, and a slight increase in the fraction of high angle grain boundaries was observed. On annealing samples at 423, 473, and 523 K, the fraction of dislocations and shallow angle grain boundaries were slightly decreased at 423 K.

At the same time, this drop is significant at the annealing temperature of 473 and 523 K, and this phenomenon can be observed from the GR angle map superimposed on the IPF map corresponding to these sample conditions (Figs. 3c–e), respectively. However, the fraction of high angle grain boundaries ($> 15°$) for these annealing conditions 423, 473, and 523 K significantly increases with increasing annealing temperature and is observed to be maximum for 473 K. The histogram showing boundary misorientation distribution (number fraction concerning misorientation

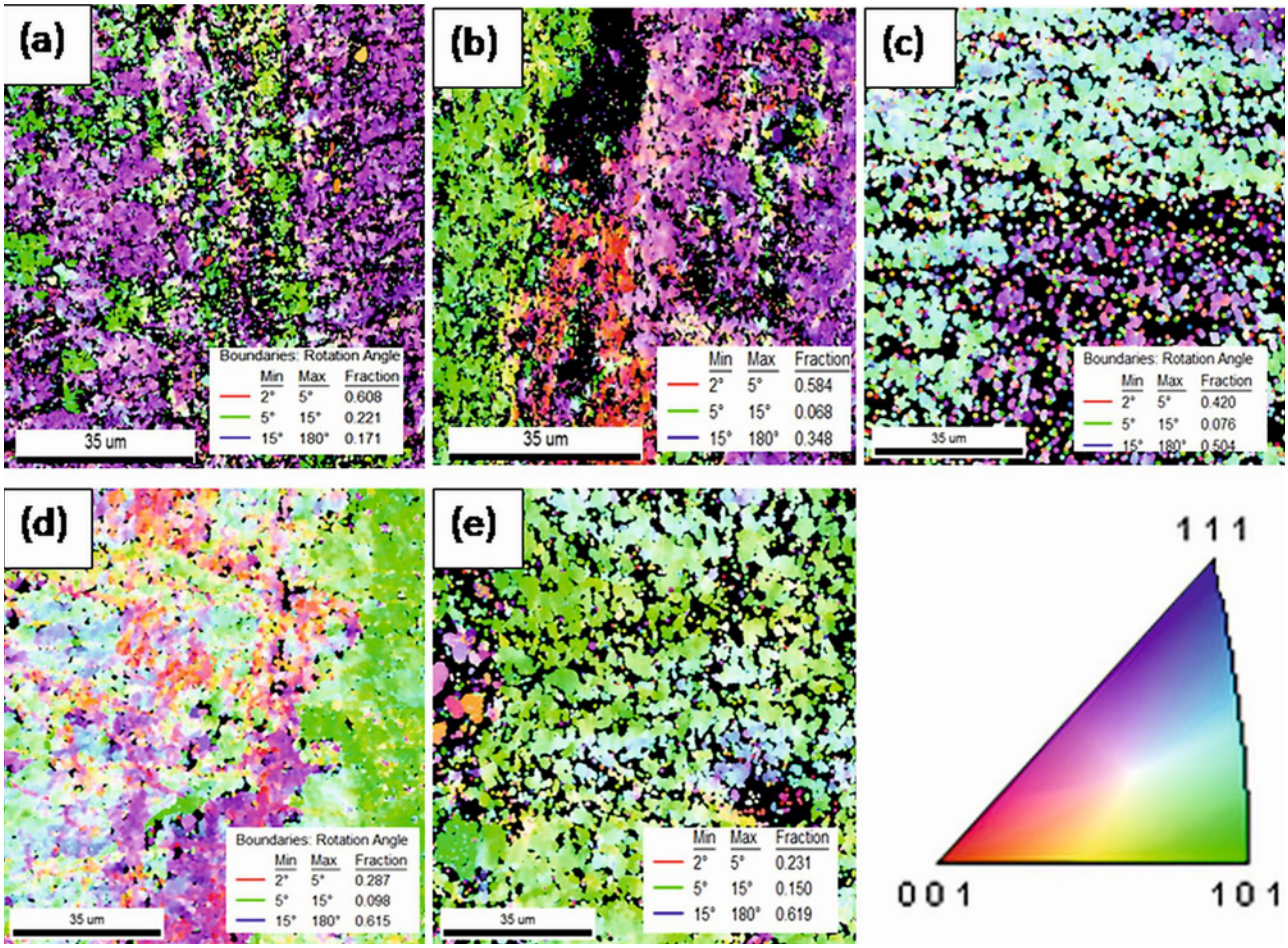

Fig. 3. The inverse pole figure (IPF) map superimposed with grain rotation (GR) angle for various processed conditions: (a) Cryorolled Al 2014 alloy (Case A), (b) Cryorolled Al 2014 annealed at 273 K (Case B), (c) Cryorolled Al 2014 annealed at 423 K (Case C), (d) Cryorolled Al 2014 annealed at 473 K (Case D), and (e) Cryorolled Al 2014 annealed at 523 K (Case E).

angle) for the cryorolled and cryorolled annealed samples at 373 to 523 K is shown in Figs. 4a–d. It confirms a similar trend, as evident from the GR angle map superimposed in the IPF map in the previous figures (Figs. 3a–e).

The partition of IPF map (PIPF) is also shown in Figs. 5a–d for the cryorolled annealed samples at temperatures of 423, 473, and 523 K. The grain orientation spread (GOS) $< 1°$ is taken for evaluating the number fraction of recovered grains as discussed in [27]. Figure 5a shows the PIPF map for the cryorolled sample annealed at 373 K. It is evident from this figure that the number of recovered grains is very few for this process condition. However, with increasing annealing temperature from 473 to 523 K, the fraction of recovered grains has increased, as depicted in Figs. 5b–d corresponding to these sample conditions.

3.3. TEM studies

TEM studies were performed to investigate the microstructural changes during the cryorolling and cryorolling followed by annealing at temperatures ranging from 373 to 523 K. The microstructural features are shown in Figs. 6a–f. The cryorolled sample consists of diffused, irregular, and ill-defined grain boundaries, as observed in Fig. 5a. Dislocation tangling zone, DDW's (Dense Dislocation Walls), and fine dislocation cells are also seen in the cryorolled sample, as depicted in Fig. 6a. At annealing of 373 K, some of the dislocations are annihilated and transformed into subgrains, as noticed in Fig. 6b. However, the number of subgrains formed at this annealing condition (373 K) is minimal, substantiating that the recovery effect at this temperature is not so prominent. A very few fine spherical precipitates (which are marked by a red arrow) were also observed corresponding to this sample condition, as seen from the TEM micrograph at this condition (Fig. 6b). When the sample is annealed at 423 K, a noticeable change in the microstructure is observed (Fig. 6c). In this case, the diffused ill-defined grain boundaries formed due to heavy deformation are re-

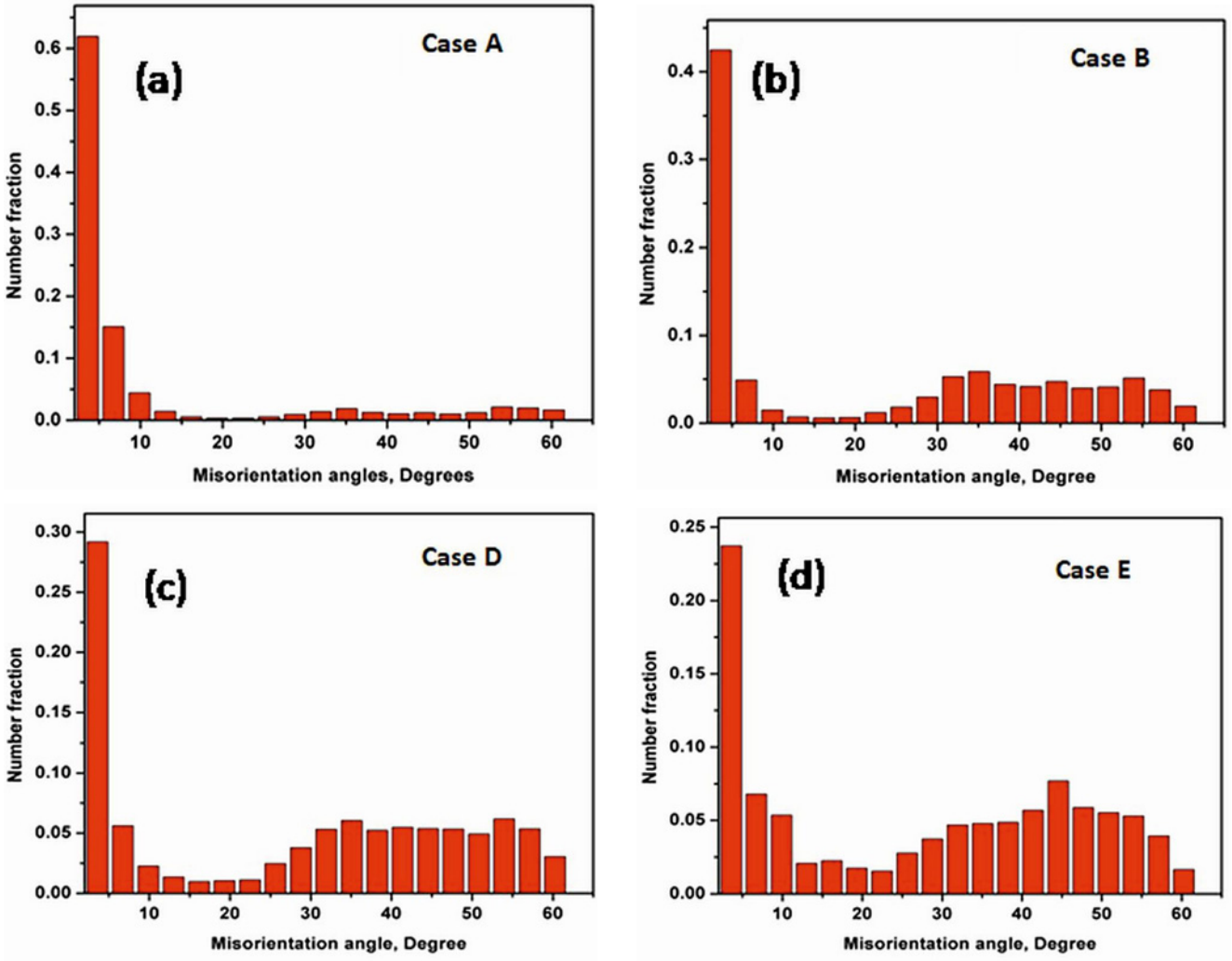

Fig. 4. Grain boundary misorientation distribution histograms for (a) Case A, (b) Case B, (c) Case D, and (d) Case E.

laxed significantly with a reduced dislocation density. Some ill-defined grain boundaries rearrange and transform into equiaxed subgrains, whose size is slightly bigger than that for the previous annealed condition. Along with equiaxed subgrain, a delicate spherical phase is still observed, somewhat coarser than the sample annealed at 1000 ℃. A substantial decrease in the dislocation density is observed when the sample is annealed at 473 K (Fig. 6d).

In addition, subgrain size has slightly increased at this condition compared to the previous annealed condition samples. Fine spherical phase is still seen at this sample condition (473 K) as before; however, the size of this phase slightly increased when compared to the sample annealed at 373 and 423 K. It can be inferred that the recovery effect at this sample condition (473 K) is accelerated, resulting in an increase in the subgrain size, fine spherical size, and reduced dislocation density. The recovery effect is further accelerated along with the sign of the recrystallization process when the samples are annealed at 523 K, as depicted in Fig. 6e. A combination of equiaxed subgrain and recrystallized grain along with reduced dislocation content can be observed in Fig. 6e, the TEM micrographs corresponding to the sample annealed at 423 K. In addition, a significant change in precipitation behavior was also noticed at this condition. Along with the spherical phase (marked with red arrows), a fine needle phase (marked with yellow arrows) is also observed, as noticed in Fig. 6e. The spherical phase becomes significantly coarser at this condition, while the needle phase was very fine as seen from the TEM micrographs corresponding to this sample condition. For better visualization of the needle and spherical phases, a high magnification TEM micrograph is also shown in Fig. 6f, corresponding to the sample annealed at 523 K.

3.4. Mechanical properties

Detailed investigation of the mechanical properties (the ultimate tensile strength, the yield strength, and

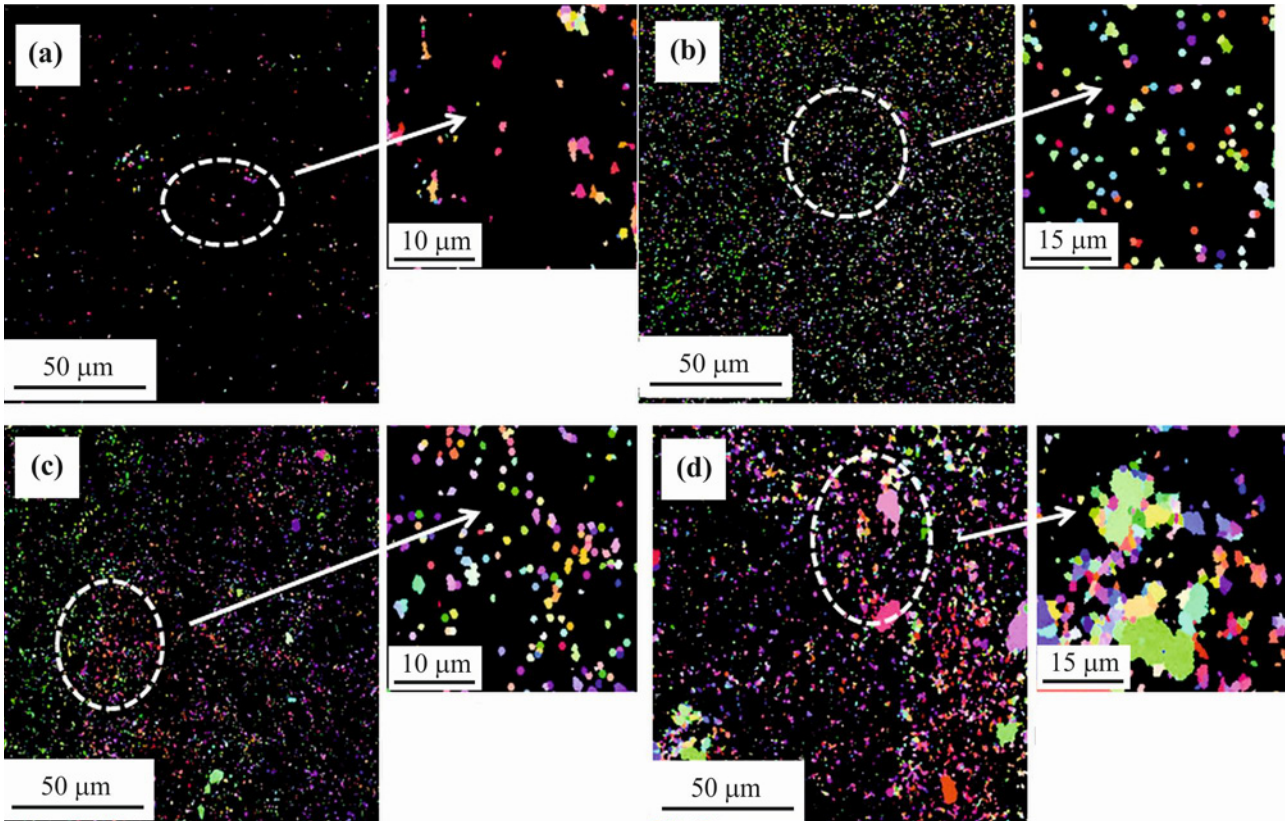

Fig. 5. The partition of IPF map (PIPF) map for (a) Case B, (b) Case C, (c) Case D, and (d) Case E.

Table 2. Mechanical properties such as tensile strength, yield strength, and hardness for solution treated and Case A to E processed alloys

Processed condition	Tensile strength (MPa)	Yield strength (MPa)	Elongation (%)	Hardness, HV
Solution treated	245	176	18.5	115
Case A	436	385	5	151
Case B	462	401	7	167
Case C	445	390	9	159
Case D	425	365	13	147
Case E	357	310	18	121

the % elongation and hardness) of the cryorolled and cryorolled annealed samples in the temperature range 373 to 523 K was reported in our earlier work [26]. These properties are listed in Table 2, and variation is depicted in Fig. 7. From Table 2 and Fig. 7, a significant improvement in the tensile strength, the yield strength, and the hardness of Al 2014 alloy after grain size reduction is observed when compared to the solutions treated alloy. On cryorolled annealed alloy in the temperature range of 373 to 523 K, improvement in the tensile and yield strength was observed. Further, between 423 to 523 K, a slight decrease in these properties was observed. However, on annealing at 473 to 523 K, a significant decrease in strength and hardness was noticed. The total % elongation of the ST alloy was observed to be 18.5 %, which is reduced to 4 % after cryorolling. In contrast, upon annealing in the temperature range of 373 to 523 K, the % elongation of the cryorolled alloy rises significantly and becomes 18 % at 523 K, as noticed in Fig. 7 and Table 2.

3.5. Fatigue crack growth rate (FCGR) test results

Fatigue life until failure is divided into two parts: (i) crack initiation life and (ii) crack propagation life. The first phase is associated with crack nucleation, and the second phase is concerned with macrocrack growth. It is imperative to identify the conditions at which the crack growth takes place before unstable failure. Sometimes, these fatigue cracks may become dangerous from the point of view of safety and the

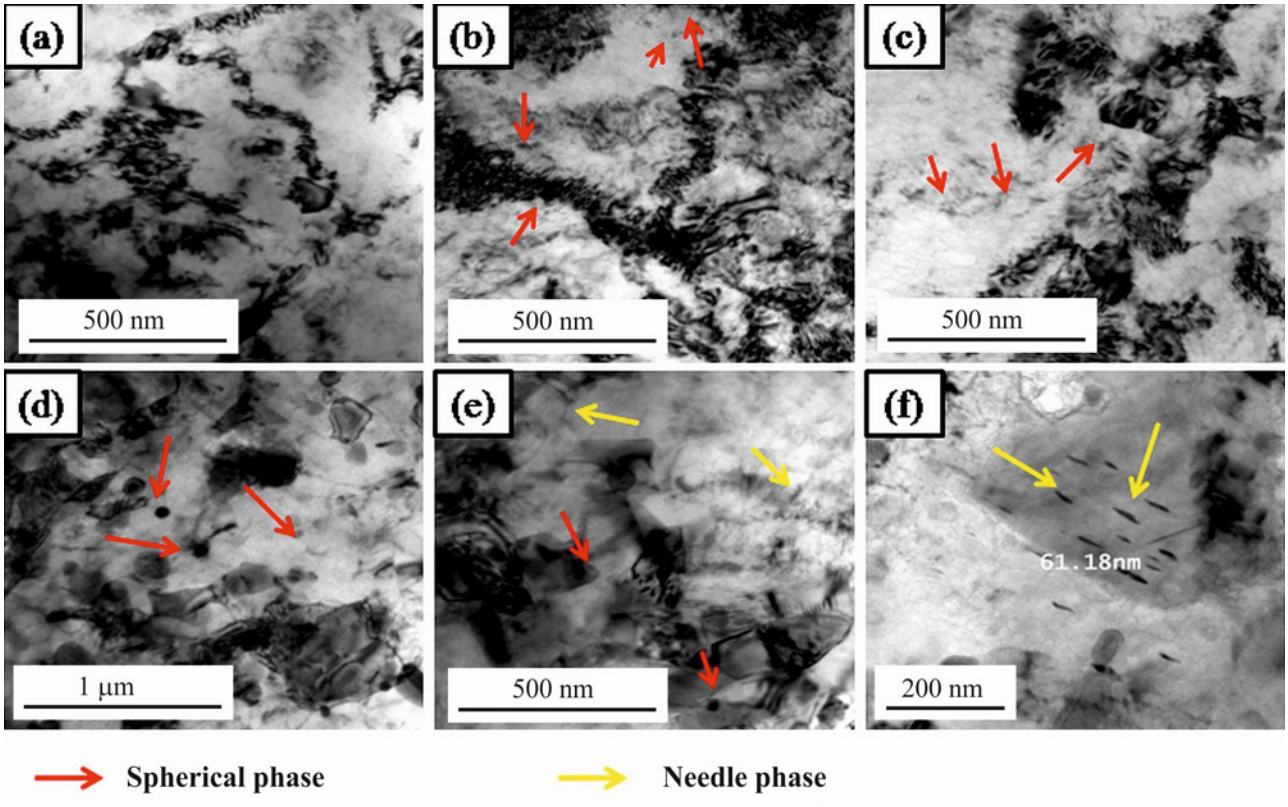

Fig. 6. TEM micrographs for various processed conditions: (a) Case A, (b) Case B, (c) Case C, (d) Case D, (e) Case E, and (f) Case E at higher magnification.

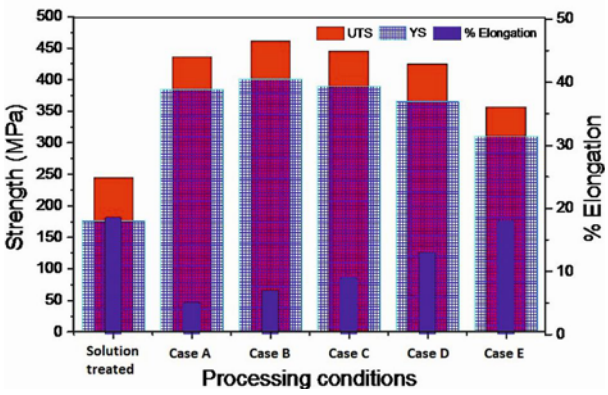

Fig. 7. Variation of tensile strength, yield strength, and % elongation with respect to various processing conditions.

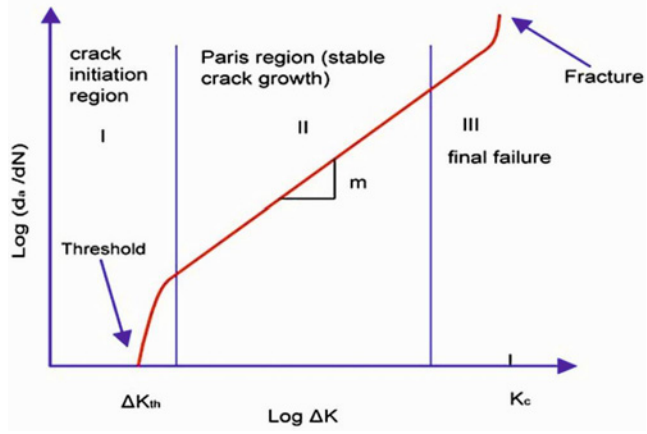

Fig. 8. Schematic showing the three stages of fatigue crack growth curve.

economy. Therefore, it is essential to monitor the fatigue crack growth through periodic inspections. A fatigue crack growth test was conducted on the solution treated, cryorolled, and cryorolled annealed samples in the temperature range of 373 to 523 K to find their crack growth resistance in this work. Usually, the FCG test results cover the ΔK and FCG rate, $\mathrm{d}a/\mathrm{d}N$. In these experiments, $\mathrm{d}a/\mathrm{d}N$ is plotted versus ΔK on a log-log plot. The following expression is used to model the different regions I, II, and III of the fatigue crack growth curve (illustrated by Fig. 8) as reported in [32]:

$$\mathrm{d}a/\mathrm{d}N = f_{\mathrm{R}}(\Delta K). \tag{6}$$

Regions I, II, and III are the threshold ΔK region, the Paris ΔK region, and the stable tearing crack growth region, respectively, as described in the literature. The threshold value of the stress intensity factor

Table 3. List of Paris constants m and constants C for solution treated and Case A to E processed alloys

Sample condition	m	C	ΔK_{th} $\left(\text{MPa}\sqrt{\text{m}}\right)$
Solution treated	3.2	4×10^{-9}	5.8
Case A	6.2	9×10^{-18}	7.17
Case B	3.5	3×10^{-7}	12.2
Case C	4.1	4×10^{-15}	8.43
Case D	5.3	8×10^{-9}	7.44
Case E	6.9	6×10^{-14}	6.35

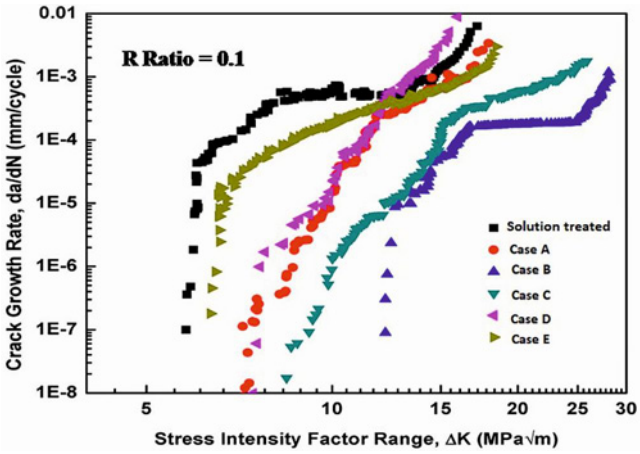

Fig. 9. Fatigue crack growth curve for various processed conditions.

in regime I is denoted by ΔK_{th} and concerned with the minimum value of the stress intensity factor below which macro crack cannot be initiated in the material.

Region II is a stable crack propagation region and can be modeled by using the following equation as described in [32]:

$$\mathrm{d}a/\mathrm{d}N = C(\Delta K)^m, \tag{7}$$

where C and m are material constants that can be obtained by linear regression of Eq. (8):

$$\log(\mathrm{d}a/\mathrm{d}N) = \log(C) + m\log(K), \tag{8}$$

where m is the slope of the Paris regime and $\log(C)$ is the intercept on the $\log(\mathrm{d}a/\mathrm{d}N)$ axis.

The crack growth rate in a stable tearing crack growth region III is too high, resulting in a tiny crack growth life with limited engineering significance. Based on the above discussion, the stage II Paris crack growth region was investigated in the temperature range of 373 to 523 K for all the processed conditions, i.e., solution treated, cryorolled, and cryorolled annealed samples. The values of constant C and m were evaluated for the above cases and are listed in Table 3. FCG rate curves for various processed conditions are shown in Fig. 9. From the analysis of the FCG rate curves, the following points can be highlighted:

(i) The FCG resistance of the bulk U.F.G. Al 2014 alloy has decreased for a given applied K range, resulting in a fatigue crack growth rate, especially at a low ΔK compared to a coarser grain counterpart (ST alloy). A significant improvement in the FCG resistance is observed on annealing of the cryorolled alloy up to a temperature range of 373 to 473 K, and the maximum value obtained at 373 K. In contrast, a decrease in the FCG resistance is observed at the annealing temperature of 523 K compared to the cryorolled samples. The samples were annealed at 373, 423, and 473 K.

(ii) The threshold intensity factor (ΔK_{th}) values are higher after cryorolling than those of the solution treated alloy.

(iii) On annealing in the temperature range of 373 to 523 K, the ΔK_{th} further increases and is observed to be maximum at 373 K when compared to the solution treated and the cryorolled alloys.

4. Discussion

4.1. Factors affecting the crack growth rate near low-intensity factor range

In the present investigation, the FCG test results for the solution treated, the cryorolled, and the cryorolled annealed samples impart two critical findings: (i) FCG resistance of bulk U.F.G. Al 2014 alloy developed by cryorolling has lower FCG resistance and higher crack initiation stress intensity factor ΔK_{th} when compared to the solution treated alloy, (ii) on annealing, the FCG resistance and crack initiation stress intensity factor ΔK_{th} have improved when compared to the solution treated and the cryorolled alloy. Additionally, these parameters are observed to be maximum for the cryorolled annealed alloy at 373 K. In this work, the crack initiation stress intensity factor is characterized by ΔK_{th} by estimating the fatigue crack growth rate at 10^{-7} mm cycle^{-1}. The values of the ΔK_{th} are listed in Table 3 for various processed conditions. The constants C and m (Paris constant) for the stage II regime for all the processed conditions

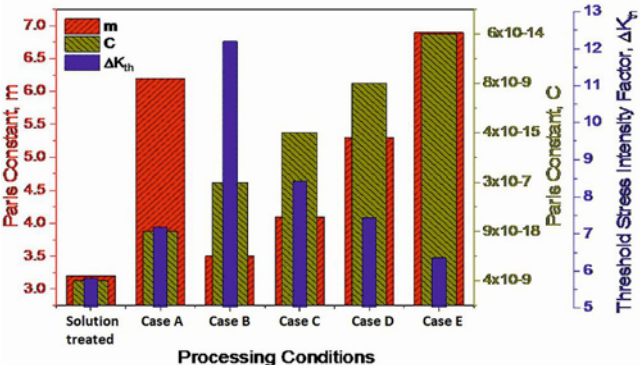

Fig. 10. Variation of Paris constant m, C, and threshold intensity factor ΔK_{th} for various processing conditions.

are evaluated as described in the previous section and shown in Fig. 10 and Table 3. Figure 9 shows the plot between the crack growth rate ($\mathrm{d}a/\mathrm{d}N$) and the ΔK for the various processed conditions in this work.

The solution treated coarse grain alloy showed a lower FCG rate and lower ΔK_{th} than the cryorolled alloy, especially for the low and moderate ΔK, as evident from Fig. 9. The observed value of Paris constant m (Fig. 10) for solution treated alloy also confirms the same as it is lower for solution treated alloy than for cryorolled alloy. This implies that the fatigue crack propagation rate in bulk U.F.G. Al 2014 alloy for the low ΔK is higher than that in the coarser grain solution treated alloy. Similar findings have been observed in various literature on the FCG behavior of bulk UFG [15, 33–35]. Recently, Yin et al. [36] found that the effect of grain size on the fatigue crack growth behavior of 2524 Al alloy revealed that the fatigue crack growth resistance deteriorated after grain size reduction well below 1 μm. The crack closure effect is higher for the coarser grain alloy when compared to the bulk UFG alloy in this study. Similar findings were reported by Meyer et al. [17] during the FCG rate testing of unprocessed and ECAP-processed Al 6061 alloy. The authors observed a less tortuous crack path for bulk UFG alloy resulting in lesser crack driving force and higher FCG rate for the bulk U.F.G. Al 6061 alloy. A similar trend is observed in the present work during the FCG rate testing of the solution treated and cryorolled Al 2014 alloy. The fractured CT samples after FCGR testing for various conditions are shown in Figs. 11a–e. Figures 11a,b are the CT samples for solution treated and cryorolled Al 2014 alloy. These figures also confirm that the fracture surface profile of the cryorolled sample is slightly flat, while the fracture surface profile of the solution treated alloy is somewhat curved. It ensures that during the fracture process, a less tortuous path is available for the cryorolled sample compared to the solution treated alloy due to fast fatigue crack propagation in the cryorolled alloy. However, it is imperative to understand the FCG mechanism microscopically for the solution treated and cryorolled alloy.

It is well established that small FCG behavior is firmly microstructure sensitive, as reported in [14]. Goto et al. [14] and Vinogradov [33] reported that crack behavior in the near-threshold slow crack growth regime is strongly microstructure sensitive, while in the intermediate regime, it is microstructure insensitive. It is reported that the growth behavior of a small fatigue crack closely depends upon the cyclic plastic zone (CPZ), which is expressed by the following equation [14]:

$$r_{\text{rp}} = \frac{1}{2\sqrt{2\pi}} \left(\frac{\Delta K_{\text{eff}}}{2\sigma_0} \right)^2, \tag{9}$$

where r_{rp} is the radius of the cyclic plastic zone near the crack tip, σ_0 is the yield stress, and ΔK_{eff} is the effective stress intensity factor range, which is equal to $U\Delta K$, where U is the crack opening ratio.

The above model developed by Goto et al. [14] predicts the growth of small cracks near the low-intensity factor range for the coarse grain solution treated alloy and the UFG CR Al 2014 alloy. From Eq. (9), it is evident that for the solution treated Al 2014 alloy with a small yield stress, the radius r_{rp} of the cyclic plastic zone will be very high.

It is reported that the roughness-induced crack closure depends upon the size of the reversible cyclic zone (RPZ) near the crack tip. When the RPZ exceeds grain size, the crack path follows an intergranular crack path, providing roughness-induced crack closure [14]. A similar pattern might occur for the coarser grain solution treated alloy because the size of its RPZ is much larger than the grain size. In addition, many neighboring grains provide sufficient plasticity to the material resulting in roughness-induced crack closure for the solution treated alloy in the low ΔK. This can be confirmed from the fractograph (Fig. 12a) corresponding to the solution treated alloy near the low ΔK. From Fig. 12a, it is clear that for solution treated alloy, the roughness induced crack closure is prominent due to large width of the cyclic plastic zone resulting into a significant crack tip plasticity. This mechanism is shown in Figs. 13a–c, where it is seen that a large number of grains are well within the cyclic plastic zone, which imparts an intergranular crack path in the coarse grain solution treated alloy (Fig. 13c).

On the other hand, the yield stress for the cryorolled alloy is higher because the radius of the cyclic plastic zone for the cryorolled alloy is small. In this case, the size of the RPZ is less than the grain size (Fig. 13a) of the material, as a result of which crack may propagate along a straight growth path, as reported in [14]. The fractograph corresponding to CR alloy near the low ΔK confirms the same trend as observed in Fig. 12b. The mechanism showing the for-

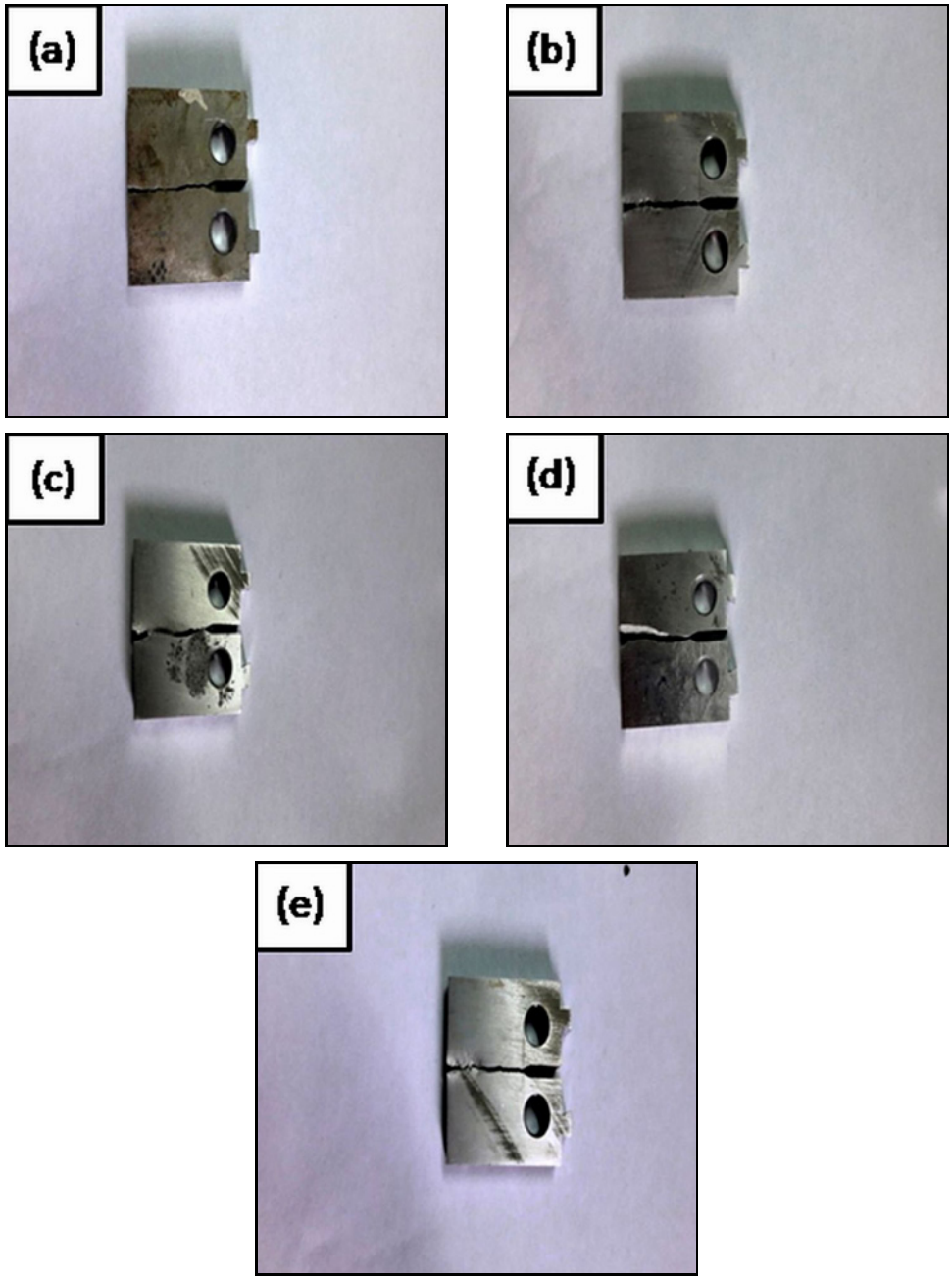

Fig. 11. Fractured compact tension (CT) sample showing the profile of fracture path for (a) solution treated Al 2014 alloy, (b) Case A, (c) Case B, (d) Case C, and (e) Case E.

mation of the cyclic plastic zone for fine grain material near a low ΔK is shown in Fig. 13a. From this figure, it is evident that for fine-grained material, the cyclic plastic zone near the crack tip is less than the grain size, which provides a less tortuous path for crack growth and reduces the crack tip plasticity, resulting in a straight crack growth path and fatigue crack growth rate near the low ΔK.

The crack growth behavior of cryorolled annealed alloy in the temperature range of 373 to 523 K is entirely different from that of the cryorolled alloy. The value of the observed Paris constant m is minimum for the cryorolled annealed alloy at 373 K; as observed from Table 3 and Fig. 10, the ΔK_{th} is the maximum for the same condition. On further annealing at higher temperatures of 423, 473, and 523 K, a slight increase in the m value and a significant drop in the ΔK_{th} (Fig. 10 and Table 3) is observed, substantiating that at low ΔK, the sample annealed at 373 K exhibits higher FCG resistance and ΔK_{th} which deteriorates when the sample is annealed at higher temperatures of 423, 473, and 523 K. The fractographs corresponding to the sample annealed in the temperature range 373 to 523 K near a low-intensity factor are shown in

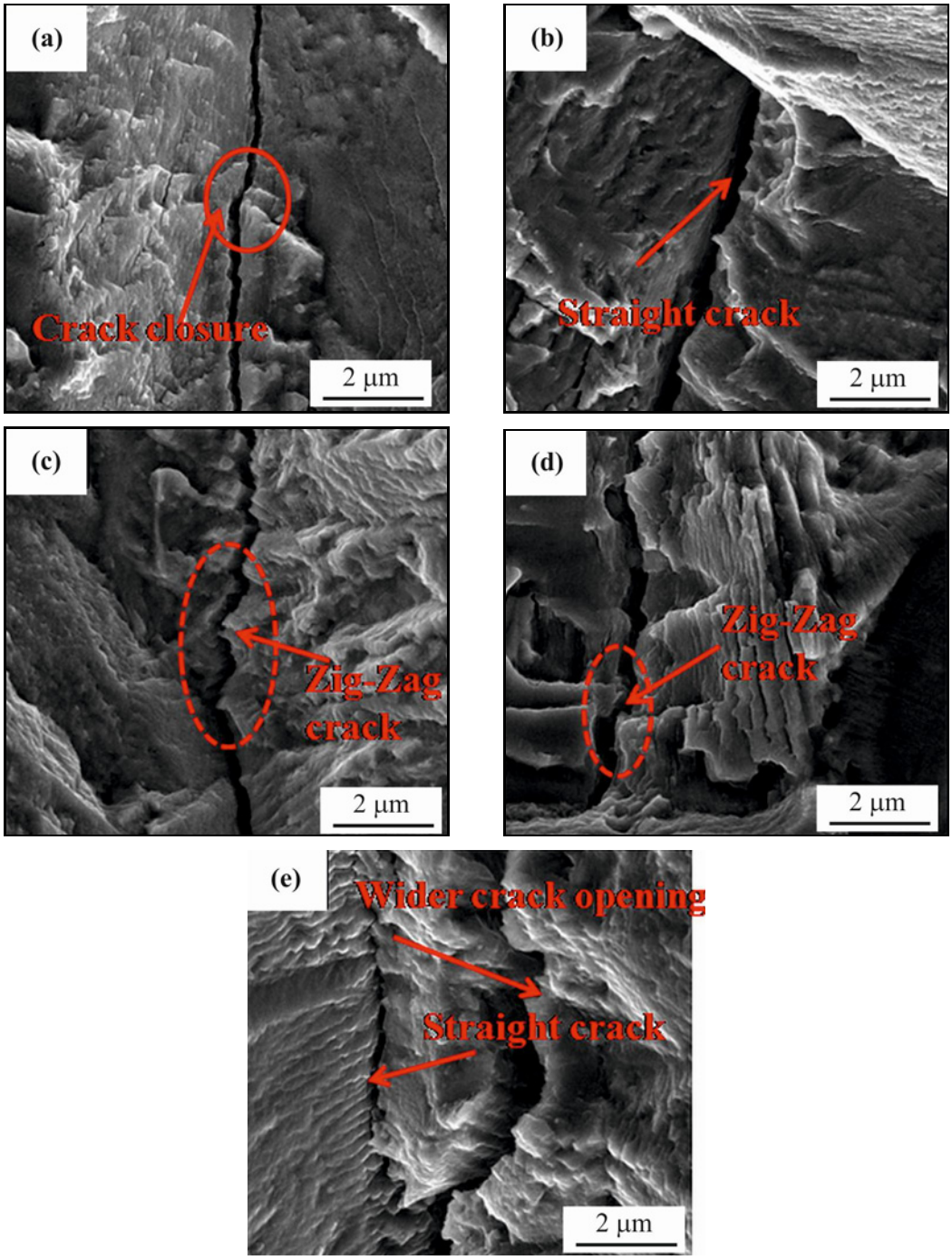

Fig. 12. Fractographs showing the crack profile near low intensity factor range for (a) solution treated Al 2014 alloy, (b) Case A, (c) Case B, (d) Case C, and (e) Case E.

Figs. 12c–e. From these fractographs, it is evident that some tightening mechanism, for example, roughness-induced crack path and serrated crack profile, is observed for the cryorolled sample annealed at 373 K (Fig. 12c). However, this feature decreases gradually when the sample is annealed at 323 and 473 K. The crack path becomes almost straight at 523 K, as observed in Figs. 12d,e. From these observations, it is clear that fatigue crack propagation for annealed alloy at 373 K is slow, showing higher crack growth resistance near the low ΔK.

On the other hand, when annealing at the temperatures of 423, 473, and 523 K, the fatigue crack propagation increases gradually, causing a decrease in FCG resistance but still more than that for cryorolled alloy. It is reported that the crack growth rate of precipitation hardenable alloy is strongly affected by the presence of shearable and non-shearable precipitates

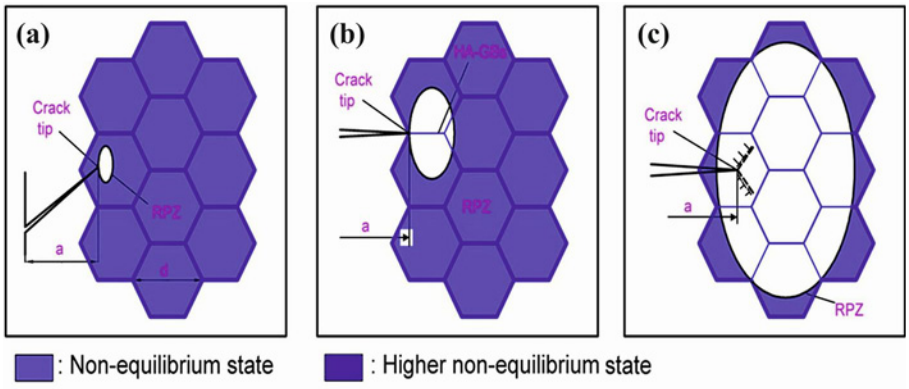

Fig. 13. Mechanism showing the relationship between cyclic reversible plastic zone (RPZ) and grain size when (a) RPZ is less than grain size; (b) RPZ is slightly greater than grain size; (c) RPZ is significantly greater than grain size.

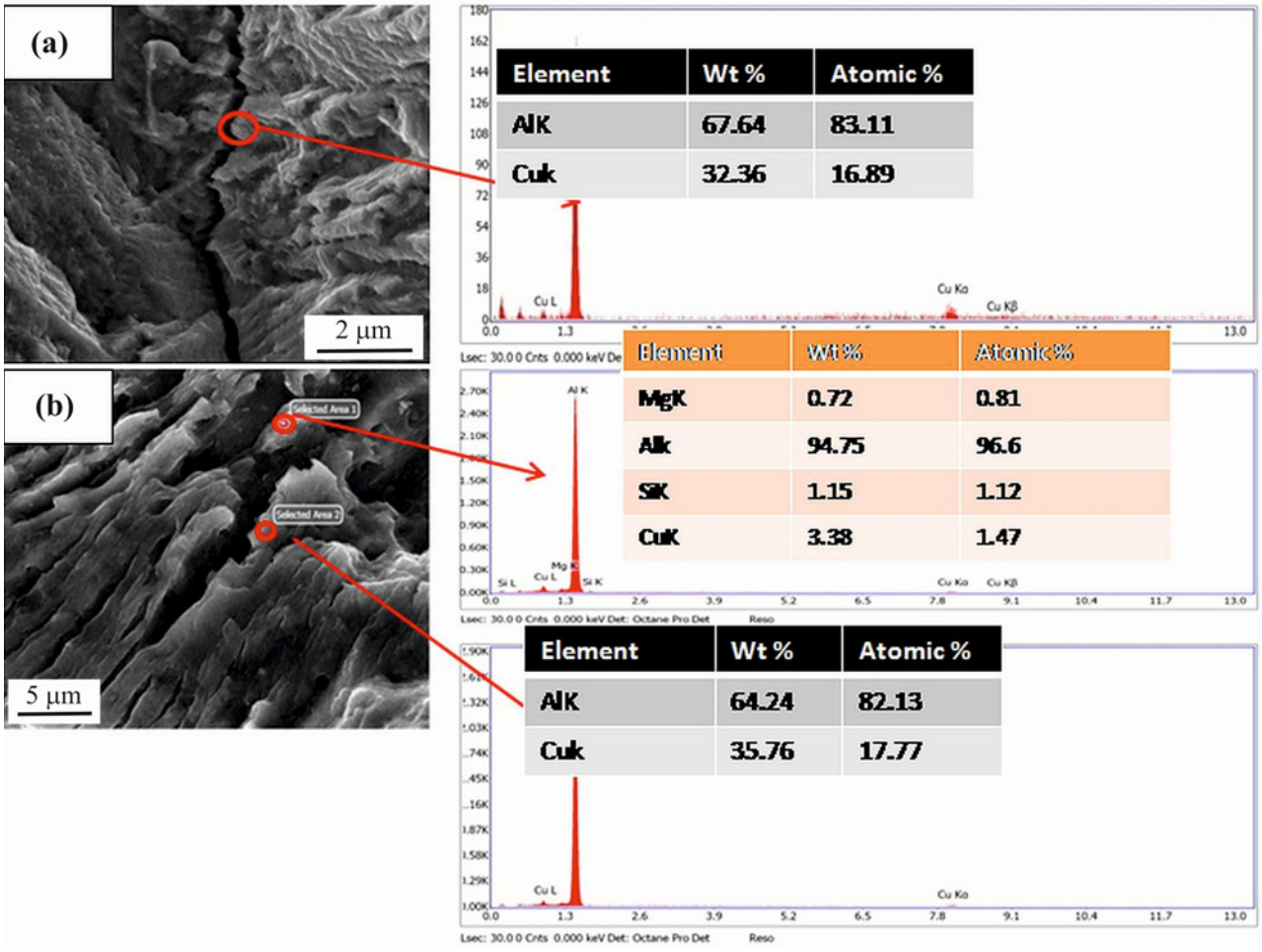

Fig. 14. EDAX of crack profile near low intensity factor range for (a) Case B and (b) Case E.

[37]. In this observation, it was found that cryorolled annealed alloy at 373 K shows higher FCG resistance not only in the low ΔK but also at the higher ΔK.

The presence of spherical and needle-like precipitates might be the possible reason for this. In our earlier work [38], various deposits were observed during post-deformation annealing in the temperature range of 373 to 523 K. The observed precipitation sequence in this temperature range has been identified as $\alpha_{sss} \rightarrow \theta' \rightarrow \theta' + \lambda'$, where α_{sss} is the supersaturated solid solution, θ' is the fine semicoherent spherical phase (Al_2Cu), and λ' is the fine semicoherent needle phase (AlCuMgSi). The θ' phase is observed in the temperature range of 373 to 473 K, while along

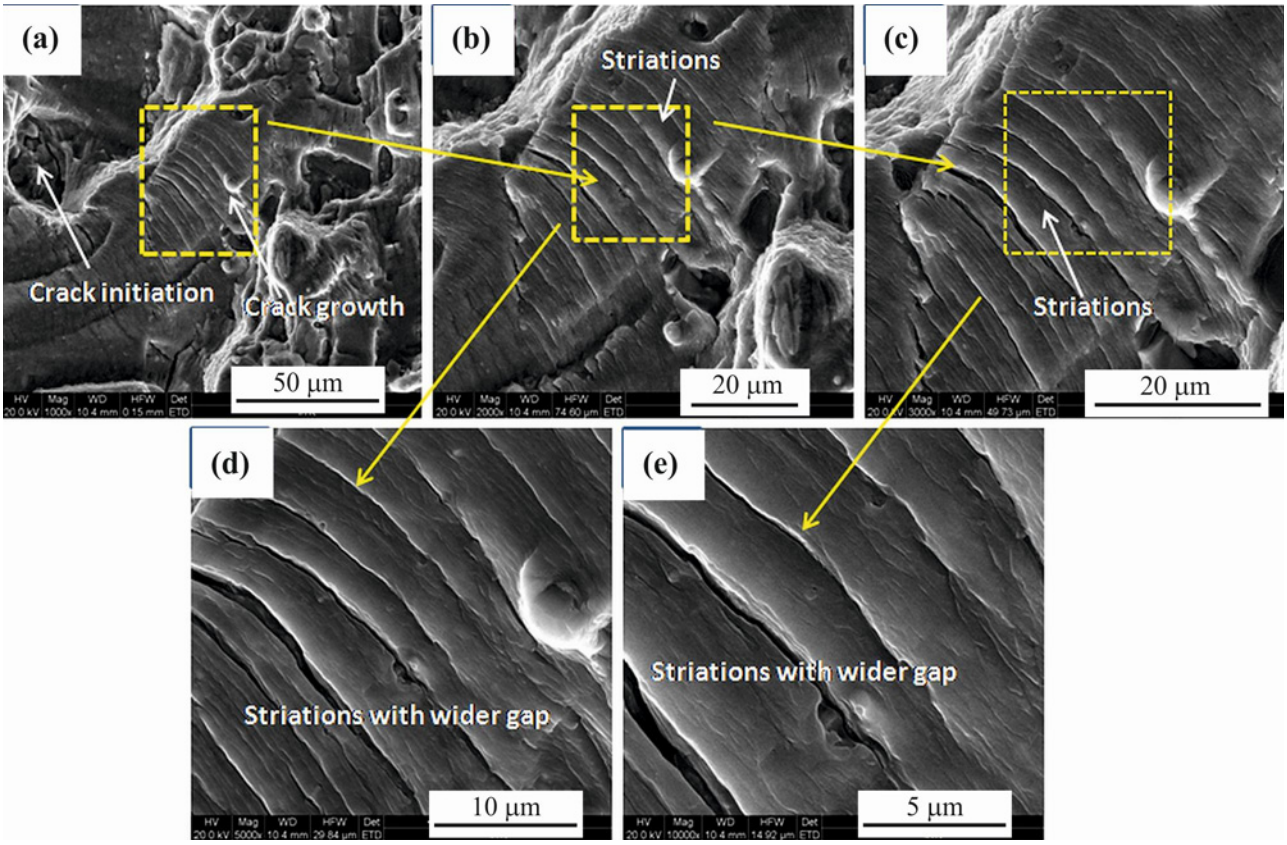

Fig. 15. Low and high magnification fractographs of solution treated Al 2014 at higher ΔK.

with θ' phase, λ' phase is observed at an annealing temperature of 523 K. In addition, with increasing annealing temperature from 373 to 523 K, these phases become slightly coarser and lose the coherency with the matrix as described in the previously published work [38].

Malekjani et al. [37] reported that precipitates' shape, size, and distribution significantly affect the material's mechanical properties. When the precipitates are coherent with the matrix, the dislocations are not cut by the fine particles and form loops around these fine coherent phases at the interface and prevent cyclic strain localization and stress concentration increasing the crack initiation life. A similar mechanism might operate in the present case for the sample annealed at 373 K. A fine semicoherent spherical phase θ' (Al_2Cu), which evolved at this temperature (373 K), forms a loop and facilitates resistance to strain localization and stress concentration, as a result of which the ΔK_{th} is observed to be maximum when compared to all other sample conditions in this work. In addition, these fine semicoherent spherical precipitates θ' (Al_2Cu) obstruct the FCG and provide significant plasticity to the crack tip, resulting in enhanced FCG resistance for the sample annealed at 373 K. Another reason for improved FCG resistance on this sample condition (373 K) might be due to the presence of planar reversible slip caused by fine semicoherent spherical phase θ' (Al_2Cu), which promotes significant zigzag crack growth along with higher crack tip deflection as reported in [37]. To confirm this, the EDAX of a crack path for the sample annealed at 373 and 523 K was carried out in this work and is shown in Figs. 14a,b. From these figures, it is evident that fine spherical phase Al_2Cu is responsible for the significant crack tip deflection and the zigzag crack growth, as a result of which FCG resistance is significantly improved for this sample condition (373 K) when compared to the rest of the processing conditions. At the annealing condition of 523 K, the spherical phase Al_2Cu and the needle phase AlCuMgSi were also observed (Fig. 14b), which provides a straight growth path during the fatigue crack propagation due to the spherical Al_2Cu phase coarsening.

With increasing annealing temperature from 373 to 473 K, the spherical phase becomes coarser gradually and loses coherency with the matrix. In addition, these coarser precipitates facilitate ease in stress concentration resulting in a gradual decrease in the crack initiation life, which reduces the ΔK_{th} gradually compared to the sample annealed at 373 K. However, the observed ΔK_{th} is still higher than that for the solution treated and cryorolled alloys because these precipitates become coarser with increasing annealing

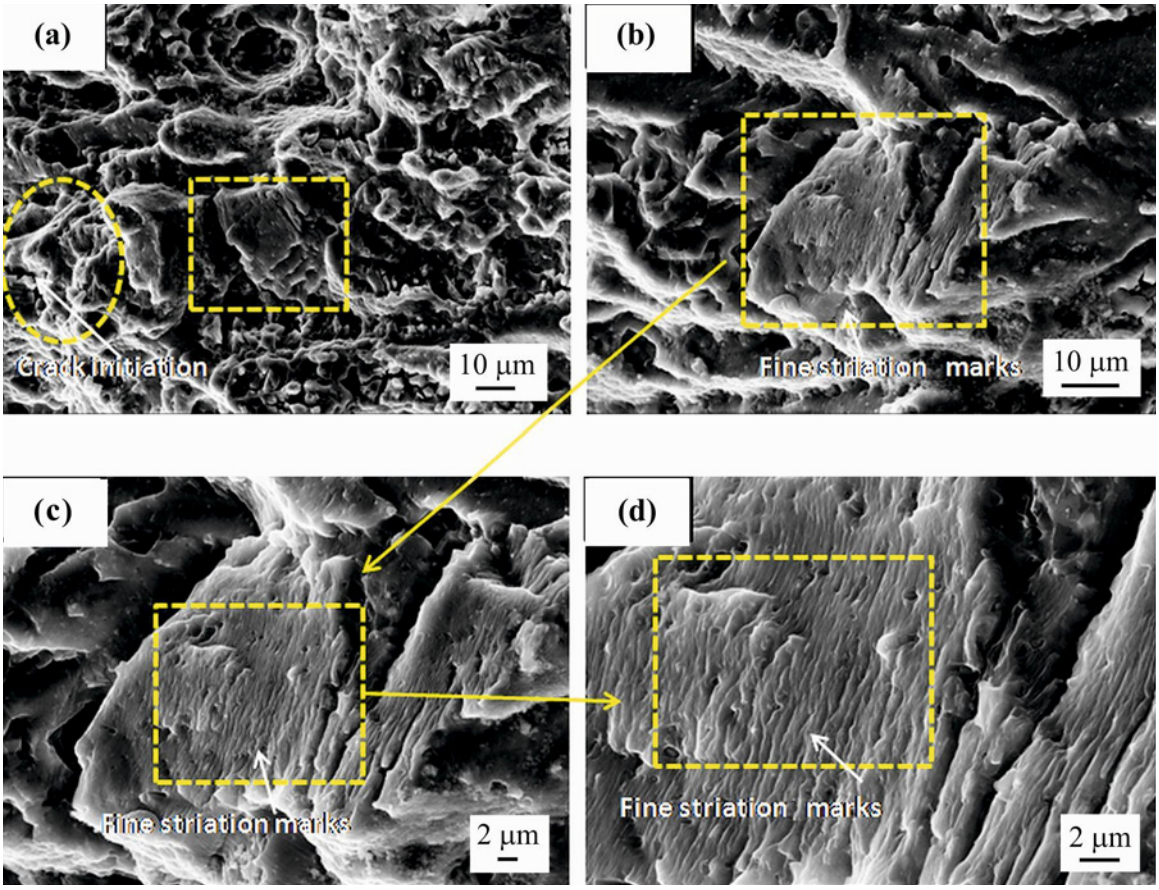

Fig. 16. Low and high magnification fractographs Case A at higher ΔK.

temperature than for the sample annealed at 373 K. However, they are still very fine and impart significant obstruction to dislocation motion. The observed ΔK_{th} is still higher than that for the solution treated and cryorolled alloys where precipitates were not evolved. FCG resistance in the temperature range from 373 to 473 K gradually decreases when compared to the sample annealed at 373 K while still more than that of the cryorolled alloy as observed in Fig. 9. With increasing annealing temperature from 373 to 473 K, the observed drop in FCG resistance when compared to sample annealed at 373 K might be due to the presence of coarser non-shearable precipitates, which does not favor planar reversible slip resulting in less crack tip deflection and less crack path tortuosity as reported in [37]. The SEM photograph (Figs. 12d,e) corresponding to the sample annealed at 423 and 523 K confirms the less crack path tortuosity and crack tip deflection when compared to the sample annealed at 373 K. The ΔK_{th} and FCG resistance of the sample annealed at 523 K are observed to be less than those of the cryorolled alloy in this work because in this sample condition, along with spherical phase θ' (Al_2Cu), fine needle phase λ' (AlCuMgSi) is also observed as seen from the TEM micrographs. The spherical phase becomes significantly coarser while the needle phase is still fine. Apart from this, recovery and recrystallization also occur at this temperature, as seen from the TEM and the EBSD studies in this work. The coarser spherical phase provides more stress concentration points, resulting from which the ΔK_{th} is observed to be less than that of the cryorolled sample. In addition, a crack can penetrate along this spherical and needle phase precipitates easily in a straight line manner, as discussed earlier, resulting in a fatigue crack growth rate compared to the rest of the processing conditions used in this work.

4.2. Factors affecting the crack growth rate at high-stress intensity factor range

Investigation of crack growth behavior of solution treated, cryorolled, and cryorolled annealed alloys in high ΔK with detailed fractographic studies was performed after the FCGR testing. Figures 15a–e show the solution treated alloy's low and higher magnification fractographs after the FCGR test. The crack initiation and the crack growth regions (rectangular yellow box) can easily be visualized from the low magnification fractograph (Fig. 15a) corresponding to the solution treated alloy. Further, the higher magnification fractographs are shown in Figs.15b–e to examine the

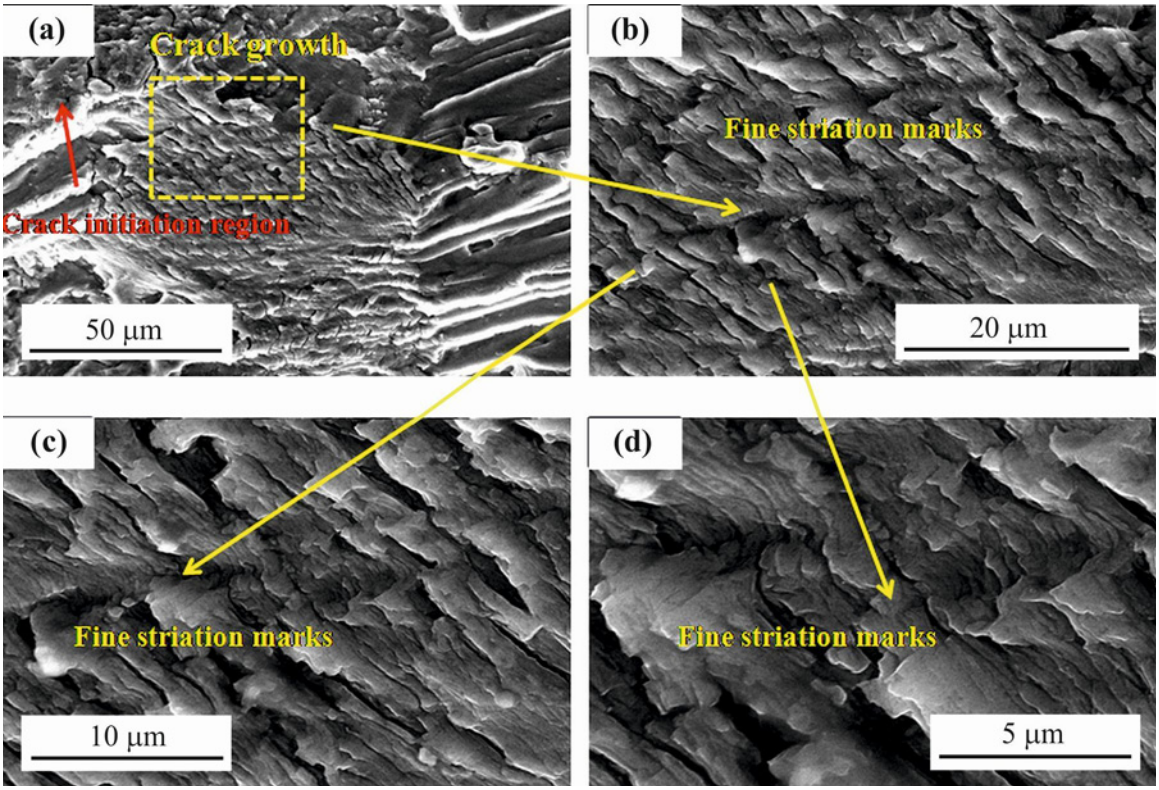

Fig. 17. Low and high magnification fractographs Case B at higher ΔK.

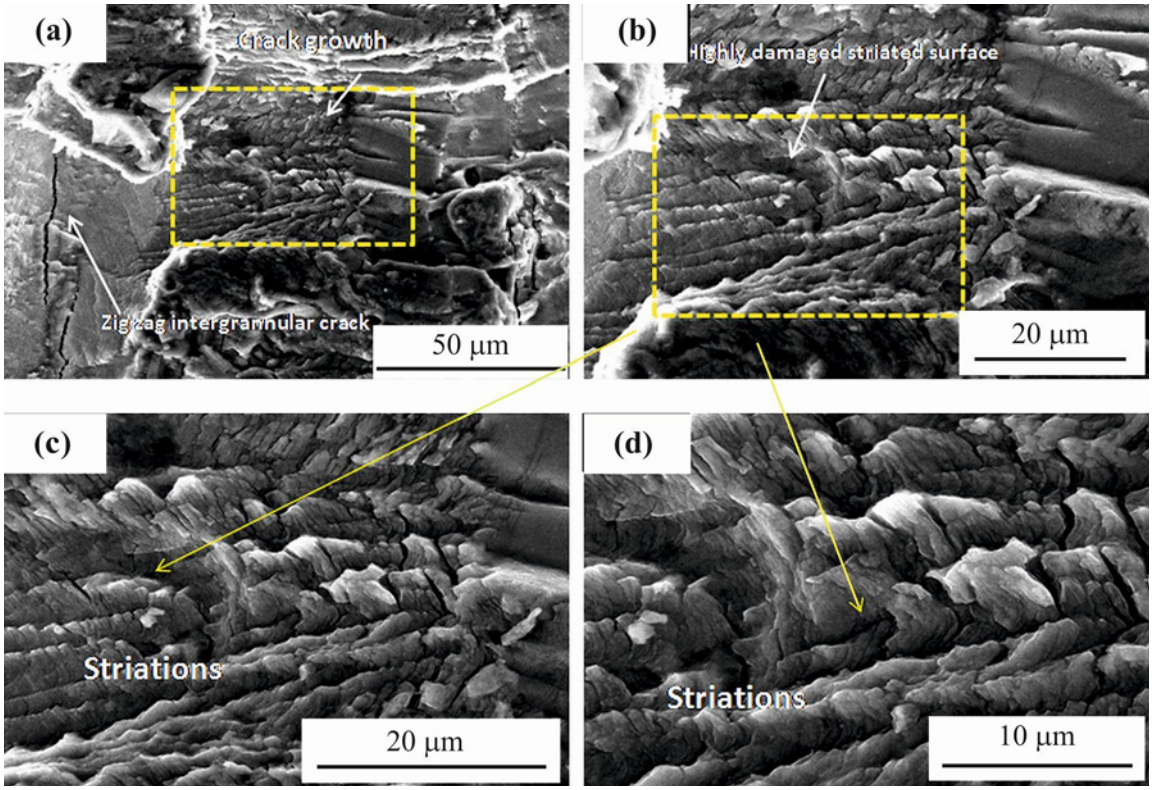

Fig. 18. Low and high magnification fractographs Case C at higher ΔK.

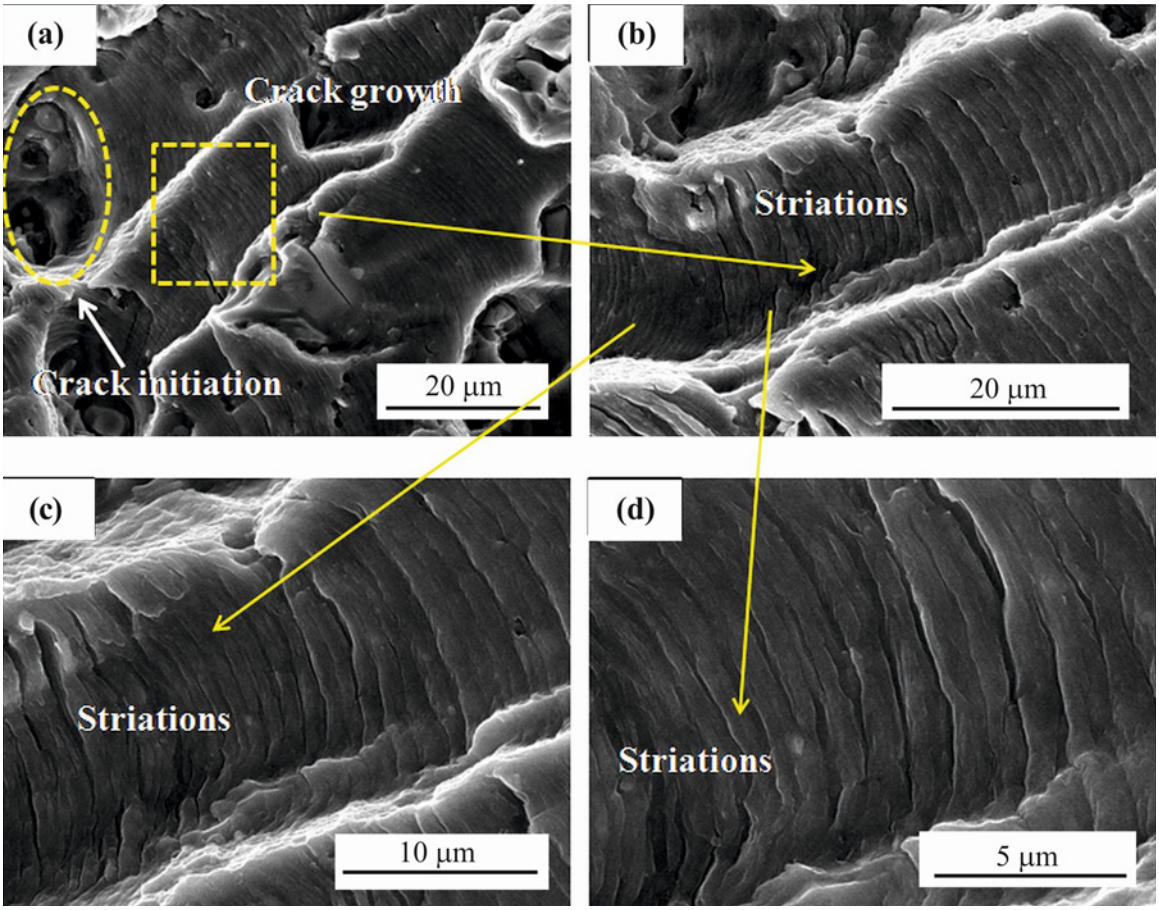

Fig. 19. Low and high magnification fractographs Case D at higher ΔK.

crack growth region more clearly. Crack growth occurs due to the formation of striations observed from these fractographs at this condition. In addition, striation with a wider gap (approximately 3 μm) is observed as noticed from the higher magnification fractograph (Fig. 15e) corresponding to this condition. It is reported that striations represent crack growth during cyclic loading [30]. The wider the striation gap, the faster the crack growth during cyclic loading [30]. For the solution treated alloy, the striation gap substantiates the fatigue crack growth in high ΔK during the FCG testing.

Figures 16a–d show the low and higher magnification fractographs corresponding to the cryorolled sample after FCGR testing. Fine striations were observed for the cryorolled sample after FCG rate testing as observed from higher magnification fractographs (Figs. 16b–d) corresponding to this sample condition. Striation width is approximately 0.20 μm as observed from the higher magnification fractograph (Fig. 16d) of the cryorolled sample, which substantiates that FCG resistance of the cryorolled sample has significantly improved when compared to the solution treated alloy in the high ΔK. Similar findings were observed by Das et al. [19] during the FCG rate testing of the cryorolled Al 7075 in high ΔK.

Fractographs corresponding to the sample annealed at 373 K are shown in Figs. 17a–d. Very fine interrupted striations were seen from higher magnification fractographs (Figs. 17b–d) corresponding to this sample condition. Interrupted striation might be due to the fine spherical semicoherent phase θ', obstructing crack propagation during the FCG testing. In addition, the striation gap is nearly 0.12 μm, corresponding to this sample condition, which is less than that of cryorolled sample, as a result of which FCG resistance of the cryorolled annealed alloy at 373 K significantly improved when compared to the previous conditions.

Figures 18a–d show the low and higher magnification fractographs of the cryorolled sample annealed at 423 K after FCG rate testing. The fracture surface for this condition is almost similar to the case of the sample annealed at 423 K. Fine interrupted striations were also observed in this sample condition. However, the striation gap is slightly more significant than the sample annealed at 373 K. The striation gap is almost 0.14 μm as observed from the higher magnification fractographs (Figs. 18b–d) corresponding to this sample condition, which means FCG resistance

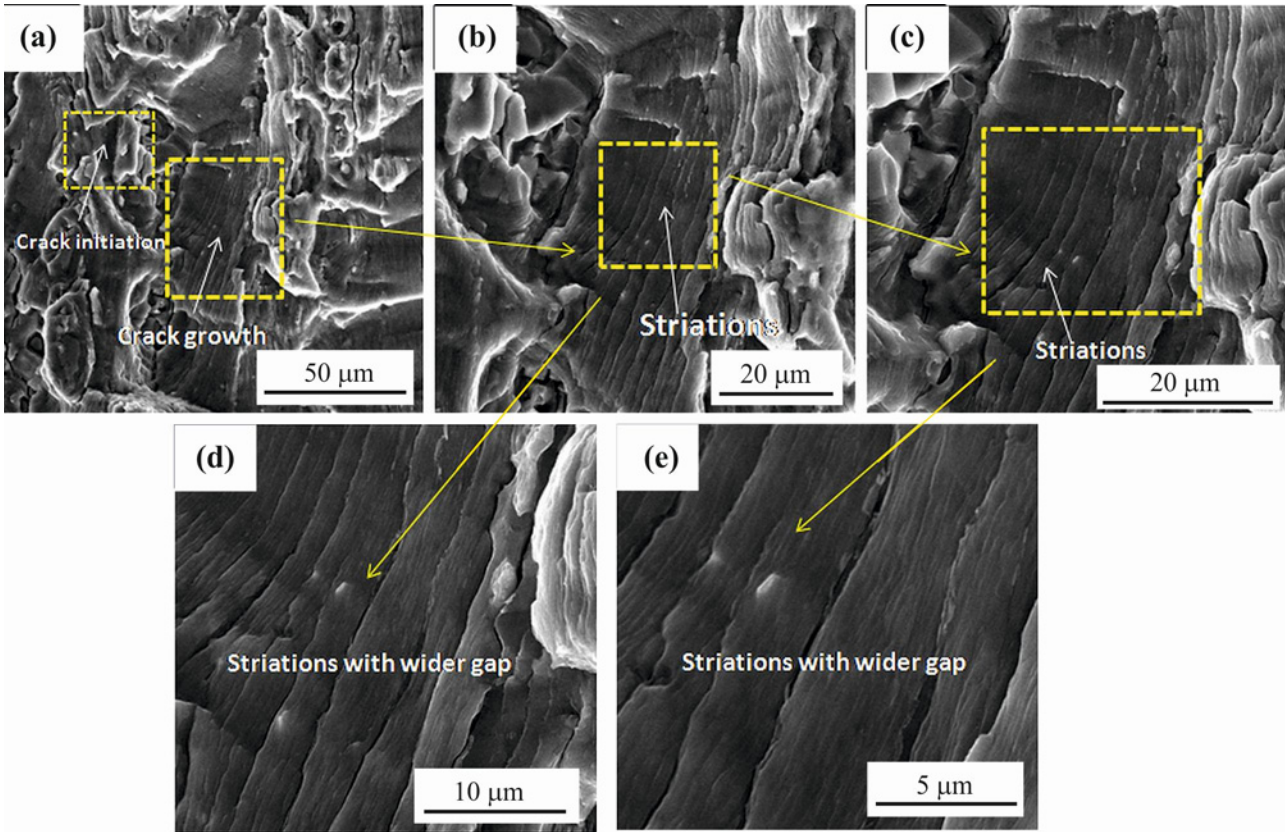

Fig. 20. Low and high magnification fractographs Case E at higher ΔK.

has slightly decreased when compared to the sample annealed at 373 K. However, the FCG resistance for the sample annealed at 423 K is still more than that of the solution treated and cryorolled samples in the high ΔK because the striation gap for this condition is less than that of the solution treated and cryorolled samples.

Figures 19a–d and Figs. 20a–e show low and high--magnification fractographs for the sample annealed at 473 and 523 K, respectively. From these fractographs, it is evident that striation width increases with increasing annealing temperature and is observed to be maximum (approximately 3 μm) for the sample annealed at 523 K, while for observed striation width for the sample annealed at 473 K is 2 μm, which indicates that FCG resistance in high ΔK range at annealing temperatures of 473 and 523 K significantly decreased and observed to be minimum for the sample annealed at 523 K.

5. Conclusions

The FCG behavior of cryorolled and cryorolled annealed Al 2014 alloy was studied in detail in the present work, and the following conclusions are as follows:

– The cryorolled Al 2014 alloy shows a fatigue crack growth rate and lower FCG resistance in the low ΔK compared to the coarse grain solution treated alloy due to the absence of a roughness-induced crack closure mechanism, which provides a less tortuous crack path during cyclic loading.

– The improvement in $\Delta K_{\text{th}}(5.8\text{MPa}\sqrt{\text{m}} - 7.17\text{MPa}\sqrt{\text{m}})$ of cryorolled Al 2014 alloy was noticed for coarser grain solution treated Al 2014 alloy. The improvement in the ΔK_{th} of cryorolled alloy is due to the formation of UFG microstructure after cryorolling.

– On annealing in the temperature range of 373 to 523 K, significant improvement in the FCG resistance of the cryorolled alloy near low ΔK is observed at 373 K because of the evolution of fine semi-coherent spherical phase, $\theta'(Al_2Cu)$, which acts as an obstacle to crack movement and provides the significant plasticity to crack tip by enhancing the size of the plastic zone near the crack tip.

– At high ΔK, FCG resistance of the cryorolled alloy is more than that of the coarser grain solution treated alloys due to the formation of very fine striations compared to the solution treated alloy.

– FCG behavior of the annealed alloy for 373 to 523 K at higher ΔK was the same as in low ΔK. On annealing in the temperature range of 373 to 523 K, FCG resistance of the annealed alloy is improved up to 473 K when compared to the solution treated and cryorolled alloy due to the formation of very fine in-

terrupted striations. Beyond this temperature, striation width increases when compared to the cryorolled sample, resulting in a decrease in the FCG resistance compared to the cryorolled alloy.

References

[1] A. Azushima, R. Kopp, A. Korhonen, D.-Y. Yang, F. Micari, G. Lahoti, P. Groche, J. Yanagimoto, N. Tsuji, A. Rosochowski, Severe plastic deformation (SPD) processes for metals, CIRP Annals 57 (2008) 716–735. https://doi.org/10.1016/j.cirp.2008.09.005

[2] Y. Estrin, A. Vinogradov, Extreme grain refinement by severe plastic deformation: A wealth of challenging science, Acta Materialia 61 (2013) 782–817. https://doi.org/10.1016/j.actamat.2012.10.038

[3] I. Sabirov, M. Y. Murashkin, R. Valiev, Nanostructured aluminium alloys produced by severe plastic deformation: New horizons in development, Materials Science and Engineering A 560 (2013) 1–24. https://doi.org/10.1016/j.msea.2012.09.020

[4] R. Valiev, A. Korznikov, R. Mulyukov, Structure and properties of ultrafine-grained materials produced by severe plastic deformation, Materials Science and Engineering A 168 (1993) 141–148. https://doi.org/10.1016/0921-5093(93)90717-S

[5] H. Mughrabi, H. W. Höppel, Cyclic deformation and fatigue properties of very fine-grained metals and alloys, International Journal of Fatigue 32 (2010) 1413–1427. https://doi.org/10.1016/j.ijfatigue.2009.10.007

[6] T. Hanlon, E. Tabachnikova, S. Suresh, Fatigue behavior of nanocrystalline metals and alloys, International Journal of Fatigue 27 (2005) 1147–1158. https://doi.org/10.1016/j.ijfatigue.2005.06.035

[7] L. Collini, Fatigue crack growth in ECAPed commercially pure UFG copper, Procedia Engineering 2 (2010) 2065–2074. https://doi.org/10.1016/j.proeng.2010.03.222

[8] D. Singh, P. N. Rao, R. Jayaganthan, Effect of deformation temperature on mechanical properties of ultrafine grained Al-Mg alloys processed by rolling, Materials & Design 50 (2013) 646–655. https://doi.org/10.1016/j.matdes.2013.02.068

[9] R. Vafaei, M. Toroghinejad, R. Pippan, Evaluation of mechanical behavior of nano-grained 2024 Al alloy during high pressure torsion (HPT) process at various temperatures, Materials Science and Engineering A 536 (2012) 73–81. https://doi.org/10.1016/j.msea.2011.12.064

[10] M. Weiss, A. S. Taylor, P. D. Hodgson, N. Stanford, Strength and biaxial formability of cryorolled 2024 aluminium subject to concurrent recovery and precipitation, Acta Materialia 61 (2013) 5278–5289. https://doi.org/10.1016/j.actamat.2013.05.019

[11] P. Cavaliere, Fatigue properties and crack behavior of ultra-fine and nanocrystalline pure metals, International Journal of Fatigue 31 (2009) 1476–1489. https://doi.org/10.1016/j.ijfatigue.2009.05.004

[12] H. Höppel, Z. Zhou, H. Mughrabi, R. Valiev, Microstructural study of the parameters governing coarsening and cyclic softening in fatigued ultrafine-grained copper, Philosophical Magazine A 82 (2002) 1781–1794. https://doi.org/10.1080/01418610208235689

[13] H. Höppel, M. Kautz, C. Xu, M. Murashkin, T. Langdon, R. Valiev, H. Mughrabi, An overview: Fatigue behaviour of ultrafine-grained metals and alloys, International Journal of Fatigue 28 (2006) 1001–1010. https://doi.org/10.1016/j.ijfatigue.2005.08.014

[14] M. Goto, S. Han, K. Euh, J.-H. Kang, S. Kim, N. Kawagoishi, Formation of a high-cycle fatigue fracture surface and a crack growth mechanism of ultrafine-grained copper with different stages of microstructural evolution, Acta Materialia 58 (2010) 6294–6305. https://doi.org/10.1016/j.actamat.2010.07.051

[15] V. Patlan, A. Vinogradov, K. Higashi, K. Kitagawa, Overview of fatigue properties of fine grain 5056 Al-Mg alloy processed by equal-channel angular pressing, Materials Science and Engineering A 300 (2001) 171–182. https://doi.org/10.1016/S0921-5093(00)01682-8

[16] C. Chung, J. Kim, H. Kim, W. Kim, Improvement of high-cycle fatigue life in a 6061 Al alloy produced by equal channel angular pressing, Materials Science and Engineering A 337 (2002) 39–44. https://doi.org/10.1016/S0921-5093(02)00010-2

[17] L. W. Meyer, K. Sommer, T. Halle, M. Hockauf, Crack growth in ultrafine-grained AA6063 produced by equal-channel angular pressing, Journal of Materials Science 43 (2008) 7426–7431. https://doi.org/10.1007/s10853-008-2725-8

[18] J. Schijve, Fatigue of structures and materials in the 20th century and the state of the art, International Journal of Fatigue 25 (2003) 679–702. https://doi.org/10.1016/S0142-1123(03)00051-3

[19] P. Das, R. Jayaganthan, T. Chowdhury, I. V. Singh, Fatigue behaviour and crack growth rate of cryorolled Al 7075 alloy, Materials Science and Engineering A 528 (2011) 7124–7132. https://doi.org/10.1016/j.msea.2011.05.021

[20] S. Zakaria, A. Anasyida, H. Zuhailawati, B. Dhindaw, N. Jabit, A. Ismail, Characterization of mechanical and corrosion properties of cryorolled Al 1100 alloy: Effect of annealing and solution treatment, Transactions of Nonferrous Metals Society of China 31 (2021) 2949–2961. https://doi.org/10.1016/S1003-6326(21)65705-9

[21] X. Zheng, W. Xie, L. Zeng, H. Wei, X. Zhang, H. Wang, Achieving high strength and ductility in a heterogeneous-grain-structured CrCoNi alloy processed by cryorolling and subsequent short-annealing, Materials Science and Engineering A 821 (2021) 141610. https://doi.org/10.1016/j.msea.2021.141610

[22] Y. Wu, K. Luo, Y. Zhang, C. Kong, H. Yu, Microstructures and mechanical properties of a CoCrFeNiMn high-entropy alloy obtained by 223 K cryorolling and subsequent annealing, Journal of Alloys and Compounds 921 (2022) 166166. https://doi.org/10.1016/j.jallcom.2022.166166

[23] F. Yu, Y. Zhang, C. Kong, H. Yu, High strength and toughness of Ti-6Al-4V sheets via cryorolling and short-period annealing, Materials Science and Engineering A 854 (2022) 143766. https://doi.org/10.1016/j.msea.2022.143766

[24] S. K. Panigrahi, R. Jayaganthan, Effect of annealing on thermal stability, precipitate evolution, and mechanical properties of cryorolled Al 7075 alloy, Metallurgical and Materials Transactions A 42 (2011) 3208–3217. https://doi.org/10.1007/s11661-011-0723-y

[25] R. Jayaganthan, S. K. Panigrahi, Effect of cryorolling strain on precipitation kinetics of Al 7075 alloy, In: Materials Science Forum, Trans. Tech. Publ. 2008, pp. 911–916. https://doi.org/10.4028/www.scientific.net/MSF.584-586.911

[26] S. K. Panigrahi, D. Devanand, R. Jayaganthan, Effect of ageing on strength and ductility of ultrafine grained Al 6061 alloy, In: Materials Science Forum, Trans. Tech. Publ., 2010, pp. 303–309. https://doi.org/10.4028/www.scientific.net/MSF.633-634.303

[27] S. K. Panigrahi, D. Devanand, R. Jayaganthan, A comparative study on mechanical properties of ultrafine-grained Al 6061 and Al 6063 alloys processed by cryorolling, Transactions of the Indian Institute of Metals 61 (2008) 159–163. https://doi.org/10.1007/s12666-008-0028-z

[28] S. K. Panigrahi, R. Jayaganthan, Effect of annealing on precipitation, microstructural stability, and mechanical properties of cryorolled Al 6063 alloy, Journal of Materials Science 45 (2010) 5624–5636. https://doi.org/10.1007/s10853-010-4627-9

[29] S. K. Panigrahi, R. Jayaganthan, Effect of ageing on microstructure and mechanical properties of bulk, cryorolled, and room temperature rolled Al 7075 alloy, Journal of Alloys and Compounds 509 (2011) 9609–9616. https://doi.org/10.1016/j.jallcom.2011.07.028

[30] A. Joshi, K. Yogesha, R. Jayaganthan, Influence of cryorolling and followed by annealing on high cycle fatigue behavior of ultrafine grained Al 2014 alloy, Materials Characterization 127 (2017) 253–271. https://doi.org/10.1016/j.matchar.2017.02.003

[31] N. Kumar, S. Goel, R. Jayaganthan, H.-G. Brokmeier, Effect of grain boundary misorientation, deformation temperature and AlFeMnSi-phase on fatigue life of 6082 Al alloy, Materials Characterization 124 (2017) 229–240. https://doi.org/10.1016/j.matchar.2017.01.002

[32] J. Schijve (Ed.), Fatigue crack growth under variable-amplitude loading, Springer, 2001. https://doi.org/10.1007/978-1-4020-6808-9

[33] A. Vinogradov, Fatigue limit and crack growth in ultra-fine grain metals produced by severe plastic deformation, Journal of Materials Science 42 (2007) 1797–1808. https://doi.org/10.1007/s10853-006-0973-z

[34] T. Leitner, A. Hohenwarter, R. Pippan, Revisiting fatigue crack growth in various grain size regimes of Ni, Materials Science and Engineering A 646 (2015) 294–305. https://doi.org/10.1016/j.msea.2015.08.071

[35] H.-K. Kim, Y.-I. Lee, C.-S. Chung, Fatigue properties of a fine-grained magnesium alloy produced by equal channel angular pressing, Scripta Materialia 52 (2005) 473–477. https://doi.org/10.1016/j.msea.2015.08.071

[36] D. Yin, H. Liu, Y. Chen, D. Yi, B. Wang, B. Wang, F. Shen, S. Fu, C. Tang, S. Pan, Effect of grain size on fatigue-crack growth in 2524 aluminium alloy, International Journal of Fatigue 84 (2016) 9–16. https://doi.org/10.1016/j.ijfatigue.2015.11.011

[37] S. Malekjani, P. D. Hodgson, P. Cizek, I. Sabirov, T. B. Hilditch, Cyclic deformation response of UFG 2024 Al alloy, International Journal of Fatigue 33 (2011) 700–709. https://doi.org/10.1016/j.ijfatigue.2010.11.025

[38] A. Joshi, K. K. Yogesha, N. Kumar, R. Jayaganthan, Influence of annealing on microstructural evolution, precipitation sequence, and fracture toughness of cryorolled Al-Cu-Si alloy, Metallography, Microstructure, and Analysis 5 (2016) 540–556. https://doi.org/10.1007/s13632-016-0313-x